The complex rupture dynamics of an oceanic transform fault: supershear rupture and deep slip during the 2024 M_{w}7.0 Cape Mendocino Earthquake

Thomas Ulrich[1*], Yohai Magen[2], Alice-Agnes Gabriel[1,2]

[1]Department of Earth and Environmental Sciences,
Ludwig-Maximilians-Universität München, Munich, Germany
[2]Institute of Geophysics and Planetary Physics, Scripps Institution of Oceanography
University of California, San Diego, CA, USA

*E-mail: thomas.ulrich@lmu.de

May 9, 2025

Abstract

The December 5, 2024, M_{w}7.0 Cape Mendocino earthquake ruptured an oceanic transform fault within the tectonically complex Mendocino Triple Junction (MTJ), the most seismically active region of California and caused a soon-lifted tsunami evacuation alert. Its offshore location renders accurate analysis of source characteristics challenging. We integrate back-projection, geodetic and kinematic slip inversions, ensembles of hundreds of 3D dynamic rupture simulations, Coulomb stress modeling and regional velocity models to understand the event's rupture dynamics and implications. A preferred dynamic rupture scenario that matches seismic and geodetic observations is complex and asymmetric, despite the simple fault geometry, its extent limited by the M_{w}7.0 1994 earthquake and creeping fault portion. Driven by prestress heterogeneity and fault weakness, we find localized supershear rupture, and delayed deep slip of eastern fault portions where seismic and aseismic slip may coexist. The modest dynamic and static stress changes onto the adjacent Cascadia and San Andreas fault systems offer insight into possible future stress transfer pathways in the MTJ region. Our findings have important implications for the expected earthquake complexity at oceanic transform faults worldwide, and emphasize the need for improved offshore observations to support physics-based hazard assessment for offshore fault systems, including the MTJ.

Introduction

The December 5, 2024, M_{w}7.0 Cape Mendocino earthquake occurred within the tectonically complex Mendocino Triple Junction (MTJ), where the Gorda, Pacific, and North American plates intersect (Fig. 1a, [1]). It is the largest Californian earthquake since the 2019 M_{w}7.1 Ridgecrest mainshock, caused a soon-lifted tsunami evacuation alert

for more than 5 million people, and occurred in California's historically most seismically active region, which has experienced multiple M_{w}7+ earthquakes over the past few decades [2]. Although oceanic transform faults (OTFs) are often considered structurally simple, the MTJ appears as highly segmented, regularly hosting earthquakes with a variety of strike-slip and thrust faulting mechanisms. This complicated regional seismicity is governed by the tectonic setting of the MTJ, where deformation arises from interactions between the right-lateral Mendocino and San Andreas faults and the subducting Cascadia slab [3]. These complex forces generate regular large earthquakes along these faults, in addition to intraplate events, such as the M_{w}7.3 1980 earthquake[4].

Prior large and moderate-size earthquakes near the MTJ (Fig. 1) highlight the region's complex and poorly understood seismic and tsunami hazard. The 1992 M_{w}7.1 thrust earthquake, which generated a tsunami, and the 2021 M_{w}6.1 and M_{w}6.0 Petrolia strike-slip events exemplify the diversity of faulting styles accommodated within the MTJ's highly segmented fault system[2, 5]. In 2022, the M_{w}6.4 Ferndale earthquake propagated unilaterally to the east-northeast and caused severe damage and two fatalities in Humboldt County, likely due to directivity amplifying ground shaking in populated areas [6, 7]. The 2024 M_{w}7.0 Cape Mendocino earthquake studied here occurred in an area of cumulative Coulomb stress increase from several previous major events: the 1980 M_{w}7.3 left-lateral strike-slip earthquake to the north, the 1994 M_{w}7.0 earthquake at the transform fault to the west, and the 1992 M_{w}7.1 event at the Cascadia megathrust to the east [4, 8, 9]. Several moderate-magnitude events likely added additional complexity to the regional stress field. These include two M_{w}6.6 strike-slip earthquakes in the Gorda plate following the 1992 mainshock, possibly involving conjugate faulting [10], and the 1983 M_{w}6.1 earthquake, which may have ruptured a deeper portion of the fault zone beneath the 2024 event. Repeating earthquake analysis reveals that the easternmost section of the Mendocino Fault is at least partially creeping [11]. This creeping section may have limited the extent of the 2021 Petrolia earthquake, but it also hosted a M_{w}5.7 earthquake in 2015, indicating that seismic and aseismic slip may coexist along this segment.

A thorough understanding of the dynamics of the M_{w}7.0 2024 Cape Mendocino earthquake is crucial to not only better understand regional seismicity, structural and stress heterogeneity [12] but also the resulting stress redistribution onto two high-hazard fault systems, the Cascadia subduction zone to the North and the San Andreas transform fault system to the south [13]. However, the offshore location of the 2024 earthquake recorded solely by land-based instruments renders accurate analysis of source characteristics challenging. For example, the USGS model [14, 15], based on surface and body wave teleseismic observations and data from 7 high-rate and 23 static GNSS stations, has difficulty fitting body wave observations [16]. Given the limited instrumental resolution offshore, particularly in the near field, dynamic rupture models provide a useful tool to test the physical plausibility of candidate source models and to resolve key aspects of the rupture process that remain ambiguous in data-driven inversions.

Advancements in data-driven kinematic [15] and physics-based dynamic rupture [17–19] earthquake models now enable detailed analysis of source processes, even in offshore regions. Prior work [20–22] combined physics-based simulations with seismic and geodetic observations, and this integration of geophysical datasets with computational models allows for the resolution of complex faulting dynamics and their dynamic effects on seismic hazard. To investigate the rupture dynamics of the 2024 M_{w}7.0 Cape Mendocino earthquake and its im-

plications, we present ensembles of 3D dynamic rupture simulations informed either from geodetic or kinematic slip inversion and validated by seismic and geodetic observations, and back-projection. Our models reveal complex and asymmetric rupture dynamics including localized supershear rupture. Our preferred dynamic rupture scenario and its associated static and dynamic Coulomb failure stress changes demonstrate how stress interactions and structural heterogeneities within the Mendocino Triple Junction influence rupture propagation, slip distribution, and the subsequent stress redistribution onto the hazardous neighboring Cascadia subduction zone and San Andreas fault systems. Our findings highlight the importance of integrating physics-based models with seismic and geodetic observations to better constrain earthquake source processes, particularly in tectonically complex and offshore regions where traditional analysis methods face significant challenges.

Results

Geodetic slip model

Our static slip model (Fig. 2, Methods Sec. "Geodetic inversion") reveals a primary asperity centered approximately 30 km offshore, with a maximum slip of 1.8 m and deeper, smaller slip to the east. The model does not feature a pronounced shallow slip deficit and locates peak slip at shallow depth, 40-50 km west of the hypocenter. The calculated synthetic displacement achieves a root mean square (RMS) error of 3 mm in fitting the GNSS data. The model also satisfactorily explains the variance in the observed data, with an R^2 score of 0.8. This model is derived from a RMS geodetic inversion [23] subjected to smoothness constraints assuming a planar fault geometry delineated by relocated aftershocks and background seismicity [24]. We maximize the correlation between slip gradients and seismicity distribution, resulting in a rapid spatial decay of slip eastward toward a fault section that is densely populated with aftershocks [24] and repeating earthquakes [11], possibly indicating the transition to creeping behavior arresting rupture.

To the west of the main asperity region, the resolution of the geodetic inversion and the accuracy of aftershock locations decline significantly, providing only limited constraints on the western slip distribution. The calculated geodetic moment assuming a shear modulus of 35 GPa yields only a $M_{\mathrm{w}}6.86$ earthquake. This discrepancy between the geodetic and seismic moment magnitudes are likely attributed to the limited resolution of GNSS data for the western fault section. A significant additional moment can be accommodated west of the maximum slip asperity without substantially degrading the model-data fit, while this is not the case to the east of the asperity (Fig. S1). As we show in Methods Sec. "Ensemble and best-fitting dynamic rupture models informed from the geodetic slip model", combining this smooth geodetic slip model with the 1D USGS velocity model leads to a realistic moment magnitude in dynamic rupture simulations, which, however, fails to satisfactorily reproduce seismic observations (Fig. S2).

Kinematic slip model and back-projection

Our kinematic fault slip inversion ($M_{\mathrm{w}}7.0$, Methods Sec. "Kinematic source inversion", [15]) images a 60 km-long continuous slip asperity extending from 20 km west to 40 km east of the hypocenter (Fig. 2b, [25]). A deep slip

patch with a maximum of 1 m of slip is also imaged at depths larger than 10 km, located 40–50 km east of the hypocenter. Unlike in the static model, the kinematically imaged deep slip appears isolated from the main asperity. Rupture initially propagates bilaterally for ≈12 seconds, coinciding with a high moment release rate, and then transitions into a unilateral eastward rupture, during which slip rate amplitudes progressively decrease and rupture width narrows (Animation 1). Rupture continues to the isolated easternmost fault regions between 25-35 s before terminating.

Our kinematic inversion combines geodetic, teleseismic and regional broadband data from 108 stations (Fig. 1b) and achieves good fits (Table S1) to teleseismic body waves (Figs. S3, S4), teleseismic surface waves (Figs. S5, S6), and static GNSS recordings (Fig. 2). The agreement with strong-motion data is also reasonable (Fig. S7), considering we use a 1D crustal model (Fig. S8a) extracted from the 3D Cascadia community velocity model for P- and S-waves (v1.6,[26], hereafter referred to as CCVMv1.6). A 15 km-thick low-velocity layer in this model (Fig. S8a) provides a better kinematic fit to seismic observations than the shallower, stiffer crustal model used in the USGS inversion [15] (Fig. S9 and Table S1), which is interpolated from LITHO1.0 [27].

Our P-wave back-projection (Fig. 2, Methods Sec. "Back-projection") confirms initial bilateral rupture, and late slip to the east. The distribution of relative energy radiation aligns with the kinematically inferred rupture extent and the beampower aligns in overall shape and duration with the moment rate function of our kinematic model.

3D rupture dynamics

We perform an ensemble of 120 3D dynamic rupture simulations (Methods Sec. "Dynamic rupture modeling") to explore the role of fault stress heterogeneity, fault strength and fracture energy levels in governing dynamic rupture behavior. The complexity in our dynamic rupture models arises solely from the slip-model informed initial stress, which produces a highly heterogeneous stress distribution across the geometrically simple fault (see, e.g., Fig. S11). All other modeling assumptions are deliberately kept simple: we employ a linear slip-weakening friction law, assume a planar fault geometry, and use a simple 3D velocity model without incorporating off-fault plasticity.

The kinematic model constrains initial fault friction and stresses of the dynamic rupture model ensemble and vary only in three dynamic parameters [28]: (i) B, which modulates the potential dynamic stress drop; (ii) R, the ratio of potential dynamic stress drop to full frictional breakdown strength, which controls the relative fault strength [29]; and (iii) C, which defines the critical slip-weakening distance. We assume constant dynamic friction and constant effective normal stress below 4 km depth (Fig. S12), motivated by elevated pore fluid pressure inferences [30, 31]. We use the fault geometry from the kinematic model and a custom 3D crustal velocity model, which we extended from CCVMv1.6 [26] south of the Mendocino Transform Fault (Methods Sec. "3D velocity and 3D structural model" and Fig. S8). The resulting rupture dynamics vary substantially, with moment magnitudes ranging from 6.3 to 7.2 and considerable variations in peak moment release rates (Fig. S10), highlighting the critical role of the varying dynamic parameters. We validate all ensemble simulations against regional waveforms at nine stations (Fig. S13) and by comparison to the seismic moment rate (Fig. S10) and slip distribution inferred from the seismic-geodetic kinematic inversion (Sec. "Kinematic slip model and back-projection"), and the fit to

GNSS data (Fig. S14).

Despite the fault's geometric simplicity, the best-fitting (hereafter "preferred") model (Fig. 3) is characterized by complicated dynamics, including delayed rupture of isolated deep fault portions in the east and localized supershear propagation. It is obtained with slightly reduced prestress level compared to the directly inferred stress changes from the kinematic model (B=0.9), relatively low fracture energy G_{c} (C=0.3, leading to $G_{\mathrm{c}} = 6 \times 10^5\ \mathrm{J/m^2}$) compared to estimates from previous 3D earthquake rupture scenarios (Table S1, [32]), and relatively weak but not critically stressed faults (R = 0.7, Fig. S11), resembling earlier 3D dynamic rupture models matching interdisciplinary observations of real earthquakes (e.g. [19, 33, 34]).

In the preferred model, dynamic rupture propagates over $\sim$28 s in two main phases (Fig. 3a,e; Animation 2). A main slip patch ruptures within approximately 16 s, and corresponds to the main peak of the moment rate function. The earthquake rupture initiates bilaterally, then transitions to a unilateral eastward rupture 10 s after rupture onset, with slip deepening into the crust and reaching depths up to 25 km. Following rupture of the main asperity, the shallower portion of the fault continues propagating to slip eastward, producing moderate slip. Complex wavefield interactions lead to dynamic triggering of several eastern fault portions after 16 s rupture time.

Overall, rupture speed averages as sub-Rayleigh, but localized supershear rupture occurs (see Fig. 3a,d). The peak slip rate (Fig. 3c) averages 0.6 m/s across the slipping region and reaches a maximum of 2.5 m/s in the area of highest slip, where the eastward rupture front intersects with a free-surface reflected wave (Fig. 3a,c).

A comparison between dynamic rupture model ensembles initialized using smoother prestress with those incorporating more heterogeneous initial conditions highlights the importance of incorporating physical realism beyond data-fit metrics alone. We compare our preferred dynamic rupture scenario with the best-fitting model out of an alternative ensemble of 120 dynamic rupture models in which initial stresses are derived directly from our smoother geodetic model (see Methods Section "Ensemble and best-fitting dynamic rupture models informed from the geodetic slip model"). The preferred geodetically informed dynamic rupture simulation (Fig. S15) features comparable dynamic parameters ((B,C,R)=(1.0,0.1,0.6), i.e., slightly higher prestress heterogeneity amplitudes, smaller critical slip weakening distance and less critically stressed fault), but produces simpler rupture dynamics and a smoother moment rate history (Fig. 3e), along with increased slip to the east. The geodetically informed rupture scenario yields a poorer fit to seismic observations (Fig. S2), highlighting the important role of heterogeneity [23, 35] in data-driven models informing coseismic dynamic rupture propagation.

Both geodetic and kinematic inversions reveal a secondary slip asperity 60–70 km east of the hypocenter, at depths greater than 10 km. In the kinematic model, this feature appears disconnected from the main slip area. Our dynamic rupture simulation confirms that this low-slip region is dynamically viable and provides a physical mechanism for its delayed activation. Specifically, the preferred dynamic model dynamically triggers a secondary slip patch, which then initiates a downward-propagating front toward the deeper asperity (Fig. 3). In contrast, the geodetically informed dynamic model proposes an alternative scenario in which the secondary asperity is connected to the main rupture area at depth. In both cases, rupture of the secondary feature is likely facilitated by directivity effects that focus seismic energy into the eastern fault system.

Discussion and Conclusions

Structural complexity near the MTJ and its impact on the 2024 Mendocino earthquake rupture

Accurate source characterization of the 2024 Mendocino earthquake is challenged by the one-sided seismic and geodetic networks coverage [36] but also by the lack of a 3D crustal velocity model that fully encompasses the Mendocino Triple Junction (MTJ) region [26, 37, 38, Fig. S16]. Assumptions on the crustal model crucially influence (seismic) inversions and dynamic rupture simulations, specifically, for offshore rupture with asymmetric seismic network coverage [39].

Our assumed 1D velocity structure does not fully capture the structural complexity near the Cascadia subduction zone, particularly the westward increase in crustal thickness associated with the accretionary prism (Fig. S8c). This may explain why our additional inversion assuming a larger fault (Fig. S16) images an unlikely secondary slip 40–60 km west of the hypocenter, separated by a 20 km gap from the main slip region and not detected by our back-projection (Fig. 1a).

Our study area lies at the southern edge of the CCVMv1.6 velocity model [26], with only the northern portion of the Mendocino Fault included, while the southern section of the fault, closer to the San Andreas system, falls outside the model domain. CCVMv1.6 is based on a six-unit geologic framework and incorporates a thick (up to 5 km) sedimentary wedge with shear wave speeds as low as 2 km/s overlying the Cascadia subduction interface. This sedimentary wedge, which is being laterally spread and uplifted by the northward motion along the San Andreas Fault [40], is especially broad in the southern portion near the Mendocino Fault. Together with the plunging subduction interface, these sediments produce an eastward thickening of the crust and a low-velocity upper crustal structure [12]. Extending and incorporating CCVMv1.6 into our dynamic rupture simulations (Fig. 1b) enables improved fits to long-period waveforms at regional stations (Fig. S17), while resembling the westward increase in slip depth in the kinematic model.

Rupture extend limited by the M_{w}7.0 1994 earthquake and fault creep

We place the inferred slip distribution and hypocenter of the 2024 Cape Mendocino earthquake in the context of prior large earthquakes and known regions of aseismic slip. To the west, we assess the influence of the M_{w}7.0 1994 earthquake by constructing a new finite-fault model using teleseismic body and surface wave data (Fig. S18e) and computing the resulting Coulomb stress changes. The inferred slip distribution from the 1994 event lies adjacent to that of the 2024 rupture (Fig. S18a), and suggests that the 2024 rupture terminated to the west and nucleated within a region of elevated Coulomb stress (Fig. S18b,c). To the east, rupture arrest coincides with a region densely populated by repeating earthquakes [11] (Fig. 2b,c), suggesting the presence of a velocity-strengthening fault segment possibly associated with weak, hydrous shear zones due to seawater fluid flow [41], that may have arrested this earthquake.

Possible triggered slip on the Cascadia megathrust

The USGS moment tensor solution for the 2024 Cape Mendocino earthquake includes a 13% non-double-couple (DC) component. In addition, P-wave body waveforms recorded at azimuths near 90° from the Mendocino Fault (e.g., stations BBSR, FDFM, MPG, and SDV; Fig. S3) suggest that rupture may have involved slip on a secondary fault. Triggered postseismic slip on the Cascadia subduction zone has previously been inferred following the 2022 M_{w}6.4 Ferndale earthquake [42], raising the possibility of similar intraslab-interface fault interactions during the 2024 event [43, 44].

We conduct a multi-fault kinematic inversion that images two slip patches on the Cascadia interface, one shallow and one deep (Fig. S19). This model improves the overall misfit by 10%, with enhanced fits to vertical components at regional stations (e.g., PETL) and improved alignment with P-wave body waveforms near 90° azimuth (Table S1). However, the modeled amplitudes remain underpredicted (Fig. S19). While the added slip on the Cascadia megathrust helps account for the observed non-double-couple component, the possibility that the improved fit stems from the increased flexibility of the inversion rather than physical necessity leads us to favor a simpler slip model that excludes megathrust slip.

Implications for the San Andreas Fault and Cascadia megathrust

We evaluate the dynamic and static stress changes imparted by the 2024 Cape Mendocino earthquake on two high-hazard fault systems: the Cascadia megathrust to the north and the San Andreas transform fault system to the south. Interactions among these systems and the Mendocino Triple Junction are important [13, 45], as their most recent major earthquakes, the 1700 M_{w}9 Cascadia megathrust earthquake [46] and the M_{w}7.8 1906 San Francisco earthquake [47], may have extended into the MTJ region.

Our dynamic rupture model indicates that Cascadia experienced moderate dynamic stress perturbations during the 2024 event near the Mendocino Fault and at deeper depths of 19–25 km (Fig. 4a), with peak dynamic stress changes reaching 0.5 MPa. The northern segment of the San Andreas Fault experiences higher dynamic stress changes up to 1.5 MPa. The dynamic rupture model yields predominantly negative Coulomb stress changes on the Cascadia megathrust, except in the near-trench region adjacent to the Mendocino Fault, where small positive changes (up to 0.09 MPa) are inferred. In contrast, all of the northern San Andreas Fault exhibits small positive Coulomb stress changes reaching 0.09 MPa (Fig. 4b).

Supershear rupture propagation across a geometrically simple and relatively weak Mendocino fault

Our preferred dynamic rupture model exhibits localized areas of supershear rupture velocity, faster than the S-wave velocity of the surrounding material, across 16% of the total rupture area. All well-fitting rupture models within our parameter space exhibit some supershear episodes and some with even more extensive supershear propagation, for example a model with lower fracture energy, which reaches 36% of the rupture area (Fig. S20). Waveform comparisons at strong motion stations (Fig. S21) suggest that lower overall rupture speeds yield better fits at all

stations. Nonetheless, all spontaneously propagating models in our ensemble exhibit localized supershear rupture, suggesting it is a robust feature of this event's dynamics.

Our dynamic rupture models suggest that the Mendocino Fault may be relatively weak (i.e., moderate R), but not critically stressed. The geometrically simple fault permits classical Burridge-Andrews supershear rupture nucleation [48, 49]. We assume low effective normal stress, which is consistent with recent observations from the 2022 M_{w}6.4 Ferndale earthquake, which occurred nearby in the subducted Gorda slab. Guo et al. [6] infer low effective stress in the slab crust based on high-resolution V_P/V_S tomography, and systematically low stress drops for moderate earthquakes, implying that the subducted Gorda crust-likely hydraulically connected to the Mendocino Fault system-accommodates slip under relatively low strength conditions. OTFs worldwide may be mechanically weak and capable of hosting complex, multi-stage and supershear rupture processes due to fluid-rock interactions including seawater infiltration and associated hydration processes [41], systematically reducing fault strength over a broad depth range.

Conclusions

The December 2024 M_{w}7.0 Cape Mendocino earthquake demonstrates how complex rupture dynamics can emerge from a geometrically simple oceanic transform fault (OTF) embedded within the tectonically intricate Mendocino Triple Junction with important implications for the expected earthquake complexity at OTFs worldwide. By integrating back-projection analysis, geodetic and kinematic inversions with ensembles of hundreds of 3D dynamic rupture simulations and Coulomb failure stress analysis, we identify prestress heterogeneity and fault weakness as critical factors governing rupture complexity and asymmetry manifesting as deep slip and delayed dynamic activation of eastern fault portions, multiple rupture fronts, and localized supershear propagation. Rupture extend is limited by the M_{w}7.0 1994 earthquake to the west and a potentially creeping fault portion to the east. Despite limited offshore data, our heterogeneously prestressed dynamic rupture models, combined with a detailed regionally extended 3D velocity model cannot only reproduce key seismic and geodetic observations but also mechanically validate delayed Eastern deep slip potentially penetrating the creeping fault section, observed in our kinematic inversion. Our forward and inverse models highlight the importance of heterogeneity and regionally accurate crustal structure assumptions in constraining physically plausible earthquake scenarios. The 2024 earthquake imparted modest dynamic and static stress changes onto the neighboring Cascadia and San Andreas fault systems, providing insight into possible future stress transfer pathways within the MTJ. Together, these findings advance our understanding of how complex offshore fault systems slip and highlight the need for improved offshore observations and crustal velocity models to improve the physics-based hazard assessment in the Mendocino Triple Junction and for oceanic transform faults worldwide.

Figures

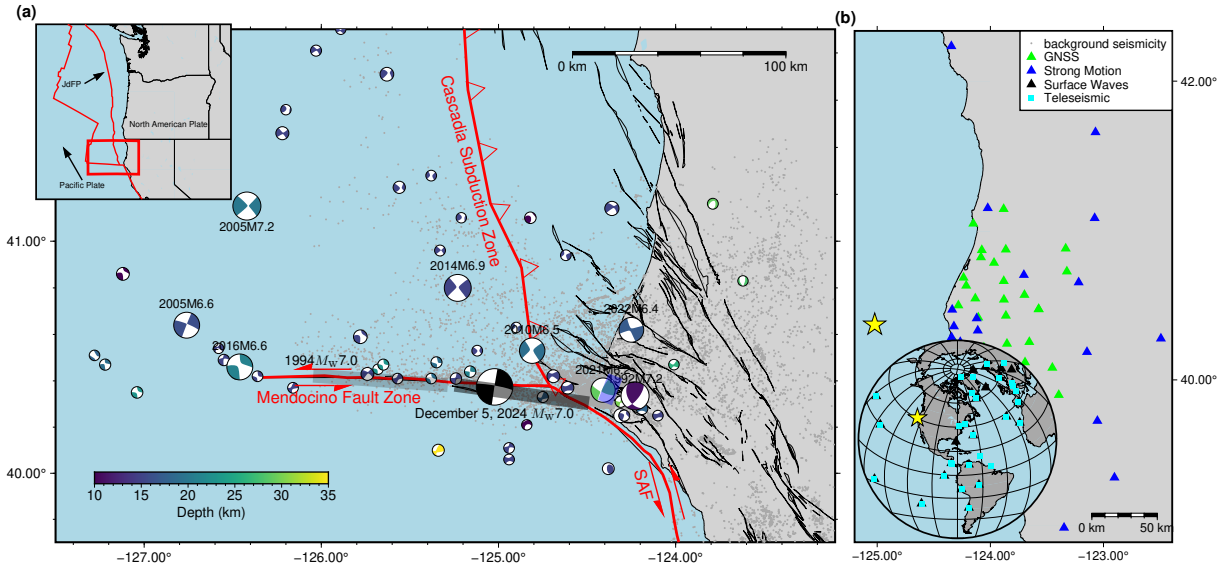

Figure 1: (a.) Tectonic setting. The main tectonic structures at the triple junction are shown in red, while the fault traces of other known faults [50] are plotted in black. Beach balls represent earthquakes with magnitudes larger than 5 [51, 52], color-coded by hypocentral depth. The most recent and significant events are labeled. The along-trace rupture extents of the 1994 and 2024 earthquakes, as constrained by our kinematic finite-fault models, are shown with light and dark shading, respectively. The blue rectangle shows the surface projection of the 1992 M7.2 earthquake [53]. Gray dots represent earthquakes with a magnitude smaller than 5 preceding the December 5 earthquake [54]. Inset: Regional view highlighting the main plate boundaries and their motion relative to the American plate. (b.) Dataset used in the kinematic inversion, which includes static displacements from 28 GNSS stations, velocity waveforms from 20 regional strong-motion accelerometers, and teleseismic recordings from 31 stations for body waves and 29 stations for surface waves.

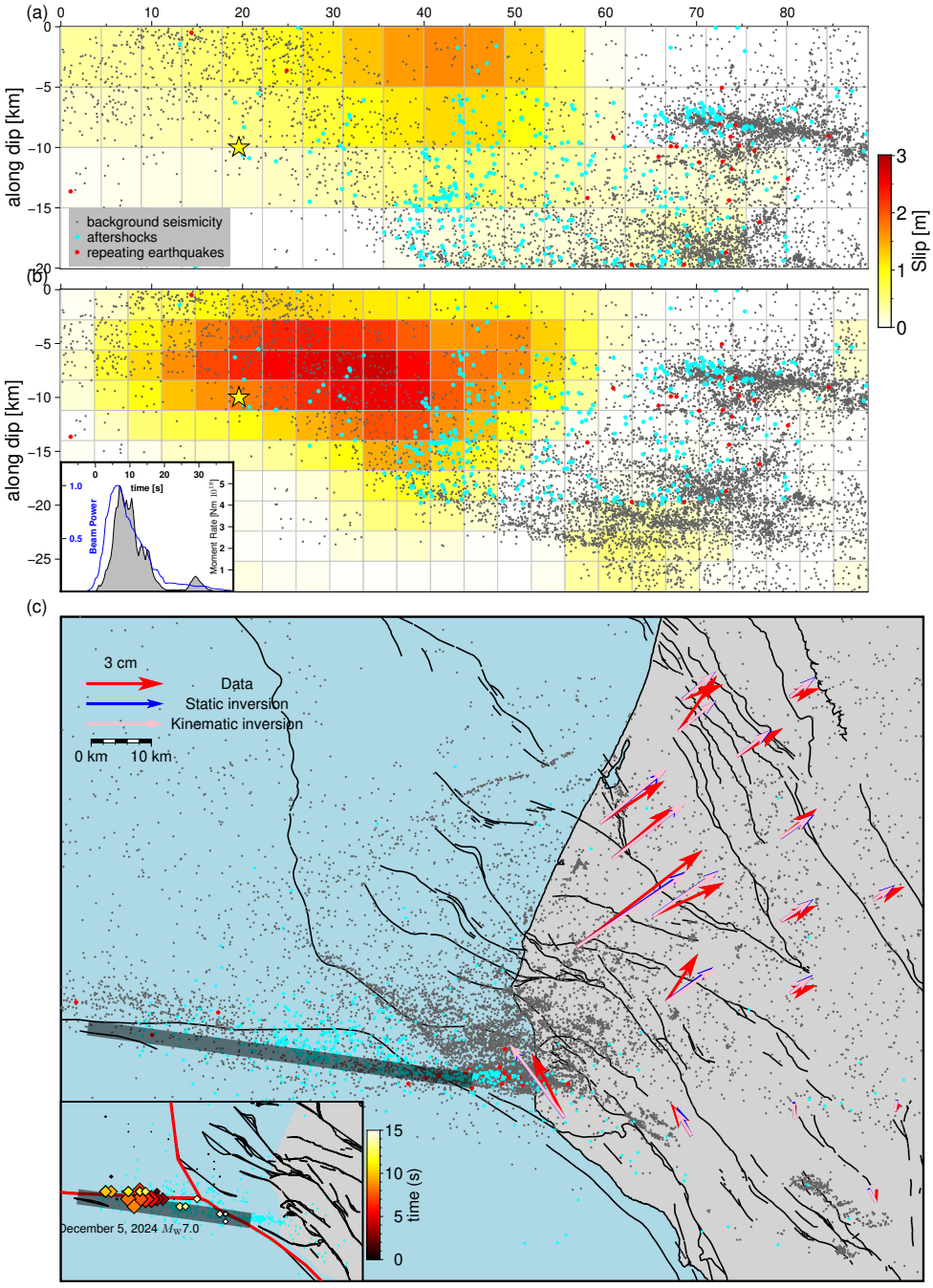

Figure 2: (a.) Slip distribution of the finite-fault model constrained using GNSS data only (static inversion). (b.) Slip distribution of the kinematic finite-fault model constrained by GNSS data, teleseismic body and surface waveforms, and regional waveforms (kinematic inversion). The inset shows the associated inferred moment rate function and the beampower from our back-projection. (c.) Horizontal co-seismic surface deformation. Blue and pink vectors represent the modeled static and kinematic inversion horizontal displacements, respectively. Red vectors show Nevada Geodetic Laboratory processed data [55]. The figure also includes relocated aftershocks (cyan dots) [24], background seismicity (black dots) [54], repeating earthquakes (red dots) [11], known fault traces [50], and the fault slip region from our kinematic finite-fault model (shaded area). Inset: Back-projection (0.25-1 Hz) of the 2014 M7.0 Cape Mendocino earthquake.

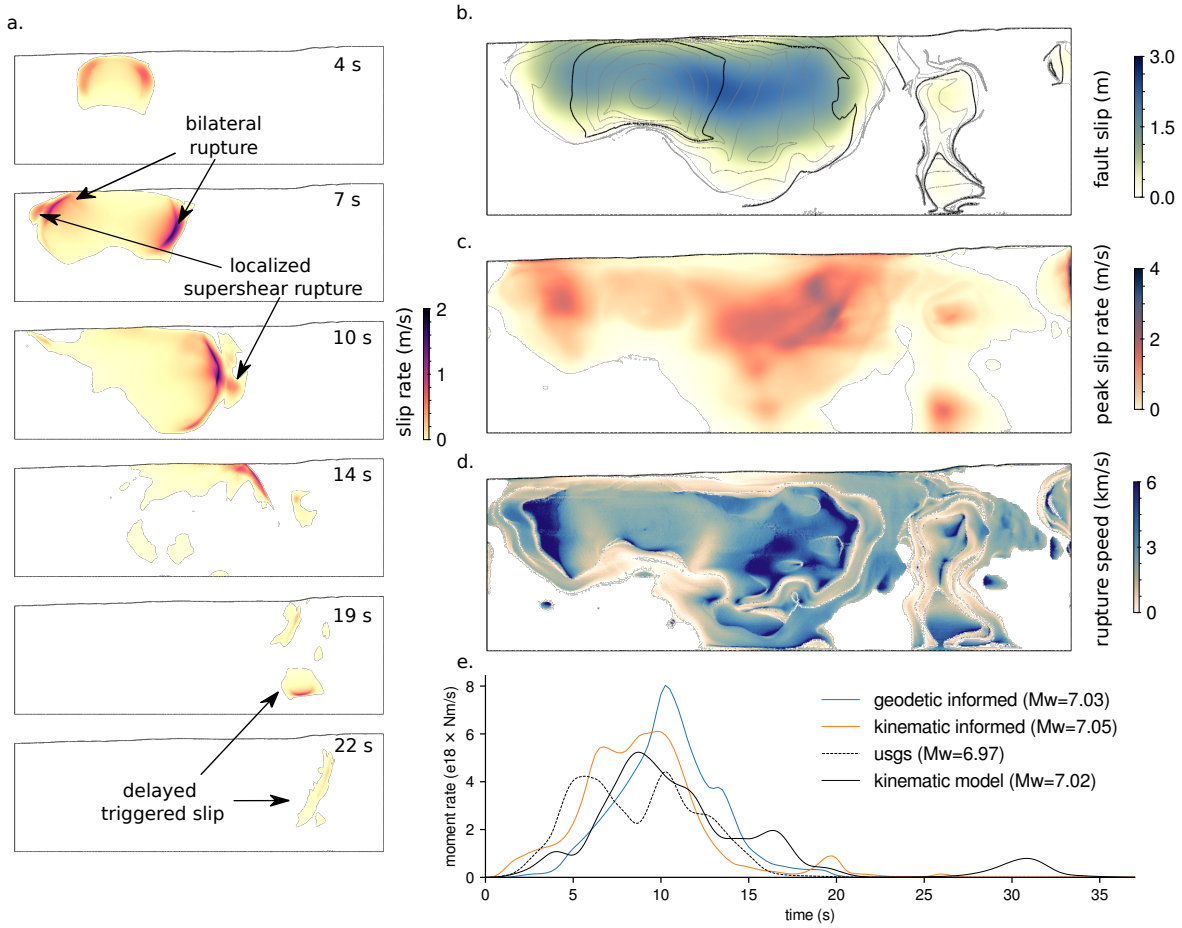

Figure 3: Preferred 3D dynamic rupture scenario, informed from our kinematic model, with parameters (B, C, R) = (0.9, 0.3, 0.7). Initially, rupture propagates bilaterally, quickly spanning a depth range of 15 km. The westward rupture front terminates near the edge of the main slip patch imaged by the kinematic model about 10 s after rupture onset. The second phase, spanning 14 s – 28 s after rupture onset, is associated with two secondary peaks in the tail of the moment rate function of the dynamic rupture model. (a.) Snapshots of absolute slip rate (see also Animation 2). (b.) Total fault slip in m, and rupture time contours every s (grey) and 5 s (black). (c.) Peak slip rate in m/s. (d.) Rupture rupture speed in m/s. (e.) Moment rate function of the dynamic rupture scenario compared to our kinematic model, the USGS kinematic model [15], an alternative best-fitting 3D dynamic rupture scenario, informed from our geodetic model.

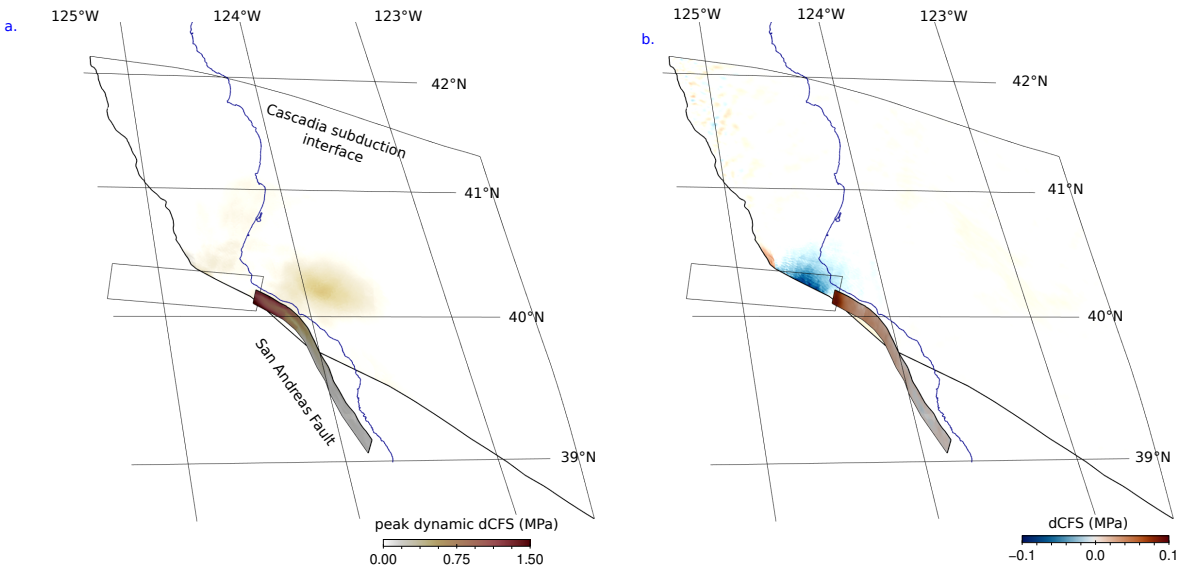

Figure 4: Peak absolute dynamic shear stress perturbation (dynΔCFS, a.) and static Coulomb failure stress changes (ΔCFS, b.) measured on the Cascadia subduction interface and the San Andreas Fault. The shear traction orientation is set to a rake of 90° for Cascadia (thrust faulting), and a rake of 180° for the San Andreas Fault (right-lateral strike-slip faulting). A static friction coefficient of 0.6 is assumed for all calculations.

Data and Resources

The three-component coseismic displacements recorded by GNSS stations processed by the Nevada Geodetic Laboratory have been downloaded from their website at http://geodesy.unr.edu/news_items/20241211/nc75095651_web.txt. The CMT solution used by the kinematic inversion and for historic earthquakes in the region was obtained from the global CMT catalog, accessed via the IRIS webpage, at https://ds.iris.edu/spudservice/momenttensor/22929936/cmtsolution.

The rapid, automatized 3D dynamic rupture simulations workflow of [56] used to build and explore an ensemble of 3D dynamic rupture models constrained by a finite fault-slip model is available at https://github.com/Thomas-Ulrich/rapid-earthquake-dynamics.git. We use v0.1.1 (https://github.com/Thomas-Ulrich/rapid-earthquake-dynamics/releases/tag/v0.1.1). The input parameters from the preferred dynamic rupture scenarios identified from this ensemble, the code used for performing the kinematic inversions, to generate the 3D velocity model, and to reproduce the manuscript figures are available at https://github.com/Thomas-Ulrich/2024CapeMendocinoEarthquake. We use WASP v1.0, with four new commits that enable a user-defined velocity model and detailed output of misfit contributions, available at https://github.com/Thomas-Ulrich/neic-finitefault/tree/Mendocino_changes. All dynamic rupture simulations were performed using SeisSol (www.seissol.org), an open-source software freely available to download from https://github.com/SeisSol/SeisSol/. We use SeisSol, v1.3.1 (https://github.com/SeisSol/SeisSol/releases/tag/v1.3.1), single precision, polynomial order p=4. Instructions for downloading, installing, and running the code are available in the SeisSol documentation at https://seissol.readthedocs.io/. Downloading and compiling instructions are at https://seissol.readthedocs.io/en/latest/compiling-seissol.html. Instructions for setting up and running simulations are at https://seissol.readthedocs.io/en/latest/configuration.html. Quickstart containerized installations and introductory materials are provided in the Docker container and Jupyter Notebooks at https://github.com/SeisSol/Training. Example problems and model configuration files are provided at https://github.com/SeisSol/Examples, many of which reproduce the SCEC 3D Dynamic Rupture benchmark problems described at https://strike.scec.org/cvws/benchmark_descriptions.html.

Acknowledgments

We thank Dara Goldberg for her guidance and support in using and extending WASP, Anthony Lomax for providing the relocated aftershock catalog using the NonLinLoc-Source-Specific-Site-Term (NLL-SSST)-Coherence (NLL-SC) method [57], and Bertrand Delouis for helpful discussions. This work was supported by Horizon Europe (grant No. 101093038, 101058129, and 101058518), NSF (grant No. EAR-2121568, EAR-2121568, OAC-2139536,OAC-2311208), NASA (grant No. 80NSSC20K0495), Schmidt Science, LLC, and the Statewide California Earthquake Center (SCEC awards 25259,25313,25341). We gratefully acknowledge the Texas Advanced Computing Center (TACC, NSF grant No. OAC-2139536), the Gauss Centre for Supercomputing (LRZ,

project pn49ha), and the Institute of Geophysics of LMU Munich [58] for providing supercomputing time.

References

1. Yeck, W. L., Shelly, D. R., Materna, K. Z., Goldberg, D. E. & Earle, P. S. Dense geophysical observations reveal a triggered, concurrent multi-fault rupture at the Mendocino Triple Junction. *Communications Earth & Environment* **4,** 94 (2023).
2. Yoon, C. E. & Shelly, D. R. Distinct Yet Adjacent Earthquake Sequences near the Mendocino Triple Junction: 20 December 2021 Mw6.1 and 6.0 Petrolia, and 20 December 2022 Mw6.4 Ferndale. *The Seismic Record* **4,** 81–92. doi:10.1785/0320230053 (2024).
3. Furlong, K. P. & Schwartz, S. Y. Influence of the Mendocino triple junction on the tectonics of coastal California. *Annu. Rev. Earth Planet. Sci.* **32,** 403–433 (2004).
4. Rollins, J. C. & Stein, R. S. Coulomb Stress Interactions among M $\geq$ 5.9 Earthquakes in the Gorda Deformation Zone and on the Mendocino Fault Zone, Cascadia Subduction Zone, and Northern San Andreas Fault. *Journal of Geophysical Research: Solid Earth* **115.** doi:10.1029/2009JB007117 (2010).
5. Hellweg, M., Dreger, D. S., Lomax, A., McPherson, R. C. & Dengler, L. The 2021 and 2022 North Coast California Earthquake Sequences and Fault Complexity in the Vicinity of the Mendocino Triple Junction. *Bulletin of the Seismological Society of America* **115,** 140–162 (2025).
6. Guo, H., Atterholt, J. W., McGuire, J. J. & Thurber, C. Evidence for Low Effective Stress Within the Crust of the Subducted Gorda Plate from the 2022 December Mw 6.4 Ferndale Earthquake Sequence. *Seismological Research Letters* (2024).
7. Hellweg, M., Dreger, D. S., Lomax, A., McPherson, R. C. & Dengler, L. The 2021 and 2022 North Coast California Earthquake Sequences and Fault Complexity in the Vicinity of the Mendocino Triple Junction. *Bulletin of the Seismological Society of America.* doi:10.1785/0120240023 (2024).
8. Hill, D. P., Eaton, J. P. & Jones, L. M. Seismicity, 1980-86. *United States Geological Survey, Professional Paper; (USA)* **1515** (1990).
9. Oppenheimer, D. *et al.* The Cape Mendocino, California, Earthquakes of April 1992: Subduction at the Triple Junction. *Science.* doi:10.1126/science.261.5120.433 (1993).
10. Velasco, A. A., Ammon, C. J. & Lay, T. Recent Large Earthquakes near Cape Mendocino and in the Gorda Plate: Broadband Source Time Functions, Fault Orientations, and Rupture Complexities. *Journal of Geophysical Research: Solid Earth* **99,** 711–728. doi:10.1029/93JB02390 (1994).
11. Materna, K., Taira, T. & Bürgmann, R. Aseismic transform fault slip at the Mendocino Triple Junction from characteristically repeating earthquakes. *Geophysical Research Letters* **45,** 699–707 (2018).
12. Furlong, K. P. & Schwartz, S. Y. Influence of the Mendocino triple junction on the tectonics of coastal California. *Annu. Rev. Earth Planet. Sci.* **32,** 403–433 (2004).
13. Rollins, J. C. & Stein, R. S. Coulomb stress interactions among M$\geq$ 5.9 earthquakes in the Gorda deformation zone and on the Mendocino Fault Zone, Cascadia subduction zone, and northern San Andreas Fault. *Journal of Geophysical Research: Solid Earth* **115** (2010).
14. Melbourne, T. I., Szeliga, W. M., Marcelo Santillan, V. & Scrivner, C. W. Global navigational satellite system seismic monitoring. *Bulletin of the Seismological Society of America* **111,** 1248–1262 (2021).
15. Goldberg, D. E., Koch, P., Melgar, D., Riquelme, S. & Yeck, W. L. Beyond the Teleseism: Introducing Regional Seismic and Geodetic Data into Routine USGS Finite-Fault Modeling. *Seismological Research Letters* **93,** 3308–3323. doi:10.1785/0220220047 (2022).
16. USGS. 2024. https://earthquake.usgs.gov/product/finite-fault/nc75095651_1/us/1733529167722/fits.zip.

17. Ando, R. & Kaneko, Y. Dynamic Rupture Simulation Reproduces Spontaneous Multifault Rupture and Arrest During the 2016 Mw 7.9 Kaikoura Earthquake. *Geophysical Research Letters* **45,** 12, 875–12, 883. doi:10.1029/2018GL080550 (2018).

18. Kyriakopoulos, C., Oglesby, D. D., Funning, G. J. & Ryan, K. J. Dynamic Rupture Modeling of the M7.2 2010 El Mayor-Cucapah Earthquake: Comparison With a Geodetic Model. *Journal of Geophysical Research: Solid Earth* **122,** 10, 263–10, 279. doi:10.1002/2017JB014294 (2017).

19. Gabriel, A.-A., Ulrich, T., Marchandon, M., Biemiller, J. & Rekoske, J. 3D Dynamic Rupture Modeling of the 6 February 2023, Kahramanmaraş, Turkey Mw7.8 and 7.7 Earthquake Doublet Using Early Observations. *The Seismic Record* **3,** 342–356. doi:10.1785/0320230028 (2023).

20. Jia, Z. *et al.* The complex dynamics of the 2023 Kahramanmaraş, Turkey, ¡i¿M¡/i¿¡sub¿w¡/sub¿ 7.8-7.7 earthquake doublet. *Science* **381,** 985–990. doi:10.1126/science.adi0685 (2023).

21. Hayek, J. N. *et al.* Non-Typical Supershear Rupture: Fault Heterogeneity and Segmentation Govern Unilateral Supershear and Cascading Multi-Fault Rupture in the 2021 7.4 Maduo Earthquake. *Geophysical Research Letters* **51.** e2024GL110128 2024GL110128, e2024GL110128. doi:https://doi.org/10.1029/2024GL110128. eprint: https://agupubs.onlinelibrary.wiley.com/doi/pdf/10.1029/2024GL110128 (2024).

22. Wang, Z. *et al.* Dynamic Rupture Process of the 2023 Mw 7.8 Kahramanmaraş Earthquake (SE Türkiye): Variable Rupture Speed and Implications for Seismic Hazard. *Geophysical Research Letters* **50,** e2023GL104787. doi:10.1029/2023GL104787 (2023).

23. Magen, Y. *et al.* Fault coalescence, slip distribution, and stress drop of the February 2023 southeast Türkiye earthquakes from joint inversion of SAR, GNSS, and burst overlap interferometry. *Seismological Research Letters* **95,** 680–696 (2024).

24. Lomax, A. *NLL-SSST-coherence High-Precision Earthquake Location Catalog for the M 7.0, 2024 Offshore Cape Mendocino, California Earthquake Sequence* 2025. doi:10.5281/zenodo.14588299.

25. USGS. 2024. https://earthquake.usgs.gov/earthquakes/eventpage/nc75095651/origin/detail.

26. Stephenson, W. J., Reitman, N. G. & Angster, S. J. *P-and S-wave velocity models incorporating the Cascadia subduction zone for 3D earthquake ground motion simulations, Version 1.6—Update for Open-File Report 2007–1348* tech. rep. (US Geological Survey, 2017). doi:10.3133/ofr20171152.

27. Pasyanos, M. E., Masters, T. G., Laske, G. & Ma, Z. LITHO1.0: An Updated Crust and Lithospheric Model of the Earth. *Journal of Geophysical Research: Solid Earth* **119,** 2153–2173. doi:10.1002/2013JB010626 (2014).

28. Weng, H. & Yang, H. Constraining frictional properties on fault by dynamic rupture simulations and near-field observations. *Journal of Geophysical Research: Solid Earth* **123,** 6658–6670 (2018).

29. Aochi, H. & Madariaga, R. The 1999 İzmit, Turkey, Earthquake: Nonplanar Fault Structure, Dynamic Rupture Process, and Strong Ground Motion. *Bulletin of the Seismological Society of America* **93,** 1249–1266. doi:10.1785/0120020167 (2003).

30. Rice, J. R. in *International geophysics* 475–503 (Elsevier, 1992).

31. Suppe, J. Fluid Overpressures and Strength of the Sedimentary Upper Crust. *Journal of Structural Geology* **69,** 481–492. doi:10.1016/j.jsg.2014.07.009 (2014).

32. Gabriel, A.-A., Garagash, D. I., Palgunadi, K. H. & Mai, P. M. Fault Size–Dependent Fracture Energy Explains Multiscale Seismicity and Cascading Earthquakes. *Science* **385,** eadj9587. doi:10.1126/science.adj9587 (2024).

33. Taufiqurrahman, T. *et al.* Dynamics, interactions and delays of the 2019 Ridgecrest rupture sequence. *Nature* **618,** 308–315 (2023).

34. Ulrich, T. *et al.* Coupled, Physics-Based Modeling Reveals Earthquake Displacements are Critical to the 2018 Palu, Sulawesi Tsunami. en. *Pure and Applied Geophysics* **176,** 4069–4109. doi:10.1007/s00024-019-02290-5 (2019).

35. Magen, Y., Ziv, A., Inbal, A., Baer, G. & Hollingsworth, J. Fault rerupture during the July 2019 Ridgecrest earthquake pair from joint slip inversion of InSAR, optical imagery, and GPS. *Bulletin of the Seismological Society of America* **110,** 1627–1643 (2020).

36. Williamson, A., Lux, A. & Allen, R. M. Performance of bEPIC Through the 2024 M 7.0 Mendocino Earthquake Sequence. *The Seismic Record* **5,** 127–135. doi:10.1785/0320250009 (2025).

37. Doody, C. *et al.* CANVAS: An Adjoint Waveform Tomography Model of California and Nevada. *Journal of Geophysical Research: Solid Earth* **128,** e2023JB027583. doi:10.1029/2023JB027583 (2023).

38. Lin, G. *et al.* A California Statewide Three-Dimensional Seismic Velocity Model from Both Absolute and Differential Times. *Bulletin of the Seismological Society of America* **100,** 225–240. doi:10.1785/0120090028 (2010).

39. Shearer, P. & Bürgmann, R. Lessons learned from the 2004 Sumatra-Andaman megathrust rupture. *Annual Review of Earth and Planetary Sciences* **38,** 103–131. doi:10.1146/annurev-earth-040809-152537 (2010).

40. Henstock, T. J. & Levander, A. Structure and Seismotectonics of the Mendocino Triple Junction, California. *Journal of Geophysical Research: Solid Earth* **108.** doi:10.1029/2001JB000902 (2003).

41. Kohli, A., Wolfson-Schwehr, M., Prigent, C. & Warren, J. M. Oceanic Transform Fault Seismicity and Slip Mode Influenced by Seawater Infiltration. *Nature Geoscience* **14,** 606–611. doi:10.1038/s41561-021-00778-1 (2021).

42. Shelly, D. R. *et al.* Subduction intraslab-interface fault interactions in the 2022 M w 6.4 Ferndale, California, earthquake sequence. *Science Advances* **10,** eadl1226 (2024).

43. Thomas, M. Y., Avouac, J.-P., Champenois, J., Lee, J.-C. & Kuo, L.-C. Spatiotemporal evolution of seismic and aseismic slip on the Longitudinal Valley Fault, Taiwan. *Journal of Geophysical Research: Solid Earth* **119,** 5114–5139 (2014).

44. Harris, R. A. Large earthquakes and creeping faults. *Reviews of Geophysics* **55,** 169–198 (2017).

45. Furlong, K. P. & Schwartz, S. Y. Influence of the Mendocino Triple Junction on the tectonics of coastal California. *Annual Review of Earth and Planetary Sciences* **32,** 403–433. doi:10.1146/annurev.earth.32.101802.120252 (2004).

46. Wang, P.-L. *et al.* Heterogeneous Rupture in the Great Cascadia Earthquake of 1700 Inferred from Coastal Subsidence Estimates. *Journal of Geophysical Research: Solid Earth* **118,** 2460–2473. doi:10.1002/jgrb.50101 (2013).

47. Song, S. G., Beroza, G. C. & Segall, P. A Unified Source Model for the 1906 San Francisco Earthquake. *Bulletin of the Seismological Society of America* **98,** 823–831. doi:10.1785/0120060402 (2008).

48. Burridge, R. Admissible speeds for plane-strain self-similar shear cracks with friction but lacking cohesion. *Geophysical Journal International* **35,** 439–455 (1973).

49. Andrews, D. Rupture propagation with finite stress in antiplane strain. *Journal of Geophysical Research* **81,** 3575–3582 (1976).

50. Jennings, C. W. & Bryant, W. A. *Fault Activity Map of California* Geologic Data Map No. 6, scale 1:750,000. Version 2.0. California Geological Survey 150th Anniversary Edition. Sacramento, CA, 2010. https://maps.conservation.ca.gov/cgs/metadata/GDM_006_FAM_750k_v2_metadata.html.

51. Dziewonski, A. M., Chou, T.-A. & Woodhouse, J. H. Determination of earthquake source parameters from waveform data for studies of global and regional seismicity. *Journal of Geophysical Research: Solid Earth* **86,** 2825–2852 (1981).

52. Ekström, G., Nettles, M. & Dziewoński, A. M. The global CMT project 2004–2010: Centroid-moment tensors for 13,017 earthquakes. *Physics of the Earth and Planetary Interiors* **200,** 1–9 (2012).

53. Murray, M. H., Marshall, G. A., Lisowski, M. & Stein, R. S. The 1992 M = 7 Cape Mendocino, California, Earthquake: Coseismic Deformation at the South End of the Cascadia Megathrust. *Journal of Geophysical Research: Solid Earth* **101,** 17707–17725. doi:10.1029/95JB02623 (1996).

54. Waldhauser, F. & Schaff, D. P. Large-scale relocation of two decades of Northern California seismicity using cross-correlation and double-difference methods. *Journal of Geophysical Research: Solid Earth* **113** (2008).

55. Blewitt, G., Hammond, W. & Kreemer, C. Harnessing the GPS data explosion for interdisciplinary science. *Eos* **99,** e2020943118 (2018).

56. Ulrich, T. & Gabriel, A.-A. *Rapid, Automatized 3D Dynamic Rupture Simulations for the Physics-Based Characterization of Large Earthquakes* 2024. doi:10.5281/zenodo.15188183.

57. Lomax, A. & Savvaidis, A. High-Precision Earthquake Location Using Source-Specific Station Terms and Inter-Event Waveform Similarity. *Journal of Geophysical Research: Solid Earth* **127.** e2021JB023190 2021JB023190, e2021JB023190. doi:https://doi.org/10.1029/2021JB023190. eprint: https://agupubs.onlinelibrary.wiley.com/doi/pdf/10.1029/2021JB023190 (2022).

58. Oeser, J., Bunge, H.-P. & Mohr, M. *Cluster design in the Earth Sciences: Tethys* in *International conference on high performance computing and communications* (2006), 31–40.

Methods

Geodetic inversion

We invert the slip distribution of the $M_{\mathrm{w}}7.0$ Cape Mendocino earthquake using static GNSS observations. We constrain the fault geometry based on relocated seismicity from the NLL-SSST-coherence catalog [24, 57, 59, 60] (Fig. 2a). To achieve an accurate slip distribution, we minimize the root-mean-square misfit between the observed GNSS displacements and model predictions, subjected to smoothness constraints to ensure physically plausible solutions. This inversion framework is expressed as:

$$\|Am - d\|_2 + \beta \|\nabla m\| \rightarrow 0\,, \tag{1}$$

where A represents the elastic Green's function matrix derived from Okada's solutions [61], m denotes the slip on fault patches, d corresponds to observed GNSS displacements, and β is a smoothing parameter that controls the trade-off between model resolution and misfit. We solve the inversion problem using the nonnegative least-squares algorithm of [62]. While a common approach is to select the smoothness parameter based on the inflection point in the misfit–versus–roughness curve, this method is not well-suited for the Cape Mendocino earthquake: the offshore location of the fault, oriented obliquely and perpendicular to the GNSS network, significantly limits fault slip resolution (Fig. S1). Therefore, we select the smoothness parameter that maximizes the alignment between the modeled slip distribution and the spatial distribution of on-fault aftershocks, ensuring that aftershocks primarily delineate the fault slip region (Fig. 2, [23]).

Kinematic source inversion

We use the Wavelet and simulated Annealing SliP inversion (WASP) workflow [15, 63], which is based on the inversion method of [64]. We rely on the automatic workflow of WASP to generate an initial model, using GNSS static data and the CMT solution [65], which we subsequently refine and update adding more observations and local constraints as explained in the following. WASP automatically constrains the fault geometry and dimensions, the number of subfaults, the ranges of fault slip amplitudes and rakes (here 170°-210°, within 20° of a rake of 190°), the rupture velocity, and the number of time windows, from fault scaling relations and the CMT solution, yielding a robust base model for subsequent manual iterations. We use only the GNSS stations in the latitude range 39.75°N-41.5°N, and with a longitude lower than -123.2°W. We update the centroid depth (initially 19 km) and the hypocentral depth (initially 0.6 km) to both equal 10 km, in agreement with the 10 km hypocentral depth and the 11.5 km depth of the W-phase moment tensor inferred by the USGS [25]. Starting from the initial model, we modify the fault geometry such that it aligns with the geodetic model. The updated fault geometry is 89 km long, and 28 km wide, dips 90° and has a strike of 96°, and is discretized into 240 3.7 km × 2.8 km subfaults, with 24 subfaults in the along-strike direction and 10 subfaults in the along-dip direction.

We refine the 1D crustal velocity model, which we find to be an important ingredient for accurately fitting teleseismic body and regional waveforms (Table S1). By default, WASP inversions are based on a 1D crustal

velocity model interpolated from the LITH1.0 global model [27] at the earthquake centroid location, atop a simplified Preliminary Reference Earth Model (PREM) global velocity model [66]. For the Cape Mendocino earthquake location, this yields a very narrow, 6-km wide 3-layer crust in the default 1D velocity model with v_p=6.2-7.7 km/s and v_s=3.6-4.4 km/s, above a stiffer 20 km layer with v_p=8.1 km/s and v_s=4.5 km/s. This 1D velocity model does not accurately represent the sedimentary wedge expected at the southern edge of the Cascadia subduction zone. We therefore use a crustal velocity model extracted from the Cascadia velocity model v1.6 (CCVMv1.6, [26]) at (-124.75°W, 40.5°N), marked by a dashed line in Fig. S8c. This coincides with the earthquake centroid location (-124.83°W, 40.4°N). Our final 1D crustal is obtained by extending the extracted profile with the same simplified global PREM model used routinely by WASP, consisting of 2 additional layers: one of 20km thickness with (v_p, v_s) =(8.1,4.5) km/s atop a layer reaching the model domain depth with (v_p, v_s)=(8.6, 4.7) km/s.

We acquire teleseismic data automatically with WASP and perform an initial kinematic inversion based on the modified fault geometry and velocity model. We then further refine the model by down-weighting three noisy stations (HRV,DWPF, and MIDW, shaded in Fig. S5 and S6), and applying the automatic "shift match" procedure in WASP, which aligns modeled waveforms with observed waveforms through cross-correlation. This correction accounts for temporal offsets that may arise due to discrepancies between the assumed 1D velocity structure and the true 3D crustal structure, as well as from uncertainties in hypocenter location and rupture onset time. At the next stage, the inversion incorporates teleseismic body waves (P and SH) and surface waves (Rayleigh and Love) data, as well as static GNSS data (Fig. 1b). We use the WASP default filtering range and data weights, that is P and SH are 1-170 s band-pass filtered, surface waves are 140-330 s band-pass filtered, and data weights decrease from surface waves to P and finally SH waves.

In the last step, we incorporate local strong-motion observations, which we select in a range of 2.5° from the hypocenter, aiming for an optimal station coverage (blue triangles in Fig. 1b). We reduce the time window for comparing ground motions and retain only the first 50 s of signal following the estimated P-wave arrival. Many regional waveforms feature long ringing coda, even at the low frequencies considered here (0.01-0.125 Hz), possibly related to resonance effects of the Cascadia subduction wedge or of the Eel river basin [67]. Our final inversion is obtained after cross-correlation and alignment of modeled synthetic waveforms with observed waveforms, acknowledging the imperfect 1D velocity model, as we did for teleseismic waveforms.

Back-projection

We image the rupture processes of the 2024 Cape Mendocino earthquake by defining a grid of potential source locations spanning 40.0°N to 40.8°N in latitude and -126.0°W to -123.5°W in longitude, with a grid spacing of 0.025° in both directions. We select a wide array of 96 stations located in Florida, Cuba, the Caribbean arc, and northern South America (Fig. S22). The broad distribution of stations, with epicentral distances ranging from 30° to 62°, provides good resolution along the rupture strike. The azimuthal coverage range, from 289° to 313°, is narrower, impacting the less critical strike-normal resolution. We use the ak135 1D velocity model [68] to compute theoretical travel times from each source grid point to the teleseismic stations. To account for travel-time biases caused by unmodeled heterogeneities using a 1D velocity structure, we apply empirical corrections

to the theoretical travel times. These corrections are estimated using a cross-correlation method applied to a 13-second time window centered on the direct P-wave arrival. To reduce the influence of low-quality signals and noise, we include only those stations where the P-wave exhibits a network-average cross-correlation coefficient greater than 0.7. The rupture process is imaged using a sliding time window back-projection technique [69, 70], with 6 s time windows and 0.5 s time steps. To maintain high wavefront coherence, we analyze low-frequency data (0.25 Hz–1 Hz). The significant location uncertainties associated with offshore events [36] prevent us from applying calibration methods (e.g., [70, 71]).

3D velocity and 3D structural model

We extend the 1 km sampled 3D Cascadia crustal velocity model ([26], CCVMv1.6), southward of the Mendocino Triple Junction (Fig. S8). Grid points initially assigned water properties, i.e., zero shear-wave velocity, are updated by replacing them with the velocity values of the first underlying grid point that has a non-zero shear-wave velocity. We then replicate the southernmost xz-slice from the model, remove the low-velocity sediments of the Cascadia accretionary prism by enforcing minimum shear and P-wave velocities of 3.1 km/s and 5.1 km/s, respectively, and shift the transect along x (west–east) to align with the coastline, distinguishing shallow oceanic crust and deeper continental crust as in CCVMv1.6 (Fig. S8).

To enable simulations of an ensemble of dynamic rupture scenarios and to evaluate both dynamic and static Coulomb stress changes on nearby high-hazard fault systems, we construct a structural model incorporating GEBCO topography and bathymetry at a resolution of 900 m, intersecting the planar fault modeling 2024 Mendocino earthquake, the Cascadia subduction interface, and the northern section of the San Andreas Fault. It spans a region of $488\times412\times200$ km³, centered on the Mendocino Fault. We employ a transverse Mercator projection centered at the epicenter location, with the following PROJ.4 definition:

```
+proj=tmerc +datum=WGS84 +k=0.9996 +lon_0=-125.02 +lat_0=40.37
```

Numerical method, computational mesh, and model resolution

We solve the spontaneous dynamic rupture and seismic wave propagation problem with high-order accuracy in space and time using the open-source software SeisSol (`https://github.com/SeisSol/SeisSol`). SeisSol uses the Arbitrary high-order accurate DERivative Discontinuous Galerkin method (ADER-DG, [72]) and end-to-end optimization for high-performance computing infrastructure [73–77]. SeisSol employs fully non-uniform, unstructured tetrahedral meshes that statically adapt to geometrically complex 3D geological structures, such as non-planar mutually intersecting faults and topography. SeisSol is verified in a wide range of community benchmarks [78] by the SCEC/USGS Dynamic Rupture Code Verification project [79].

For the ensemble dynamic rupture simulations, we use an unstructured tetrahedral mesh consisting of 1.3 million cells, resolving the Mendocino Fault with an element size of 200 m. The mesh is refined within a $140\times50\times30$ km³ region centered on and aligned with the Mendocino Fault, targeting a maximum frequency of $f_{\max} = 0.5$ Hz. Outside this region, the mesh size gradually increases to a maximum element size of 15 km.

For the preferred dynamic rupture model presented in the main text, and for the alternative 3D dynamic rupture scenario with a higher proportion of supershear rupture speed (Fig. S20), we also generate a velocity-adaptive mesh based on our extended 3D crustal velocity model from CCVMv1.6, designed for the same target frequency of $f_{\max}$ =0.5 Hz, but this time across the entire model domain. In difference to the ensemble mesh, it also resolves bathymetry and topography at a minimum of 1 km, incorporates the San Andreas Fault at a minimum resolution of 1 km and the Cascadia subduction interface at a minimum resolution of 2.5 km, resulting in a mesh with 27.0 million elements. This mesh ensures a minimum of three elements per shortest wavelength of frequency $f_{\max}$. This setup constrains numerical dispersion below the target frequency, given the five-order accuracy of the numerical scheme in both space and time, which is based on polynomial basis functions of order p = 4. Simulating 150 seconds of physical simulation time on the high-resolution computational mesh requires 6000 CPU hours on the Skylake SuperMUC-NG supercomputer (Leibniz Supercomputing Center, Germany), while the mesh used for the ensemble requires only 360 CPU hours for 30 seconds of physical simulation time.

The size of the area behind the rupture front in which shear stress decreases from its static to its dynamic value is the process zone width. In the preferred dynamic rupture models presented, we measure the median process zone width as 2840 m, while 95% of the ruptured fault elements are larger than 575 m. The recommended number of elements required to resolve the median process zone size in a dynamic rupture simulation setup without off-fault plasticity and heterogeneous initial stress conditions is 2 to 3 (for p=4) [80], thus, our rupture models are overall resolved by our chosen discretization of h =200 m, noting that each dynamic rupture element provides sub-element-resolution (25 quadrature points per cell).

Dynamic rupture modeling

We constrain 3D dynamic rupture models from the slip distributions of the geodetic and kinematic fault slip models (Fig. 2a,b). To this end, we adapt the rapid, automatized 3D dynamic rupture simulations workflow of [56] to construct an ensemble of 3D dynamic rupture models. We identify a preferred dynamic rupture model for both finite-fault models by comparing the seismic moment rate function, using the normalized cross-correlation coefficient at zero lag, and the slip distribution of the respective reference model, and by aiming to match regional waveforms. For the latter, we use the time-frequency misfit[81, 82] computed on velocity waveforms filtered between 4–60 s at nine stations (Fig. S13), using a 70 s time window starting from rupture onset.

Our workflow includes the following steps: (i) construction of a 3D structural model that integrates all considered faults and surface topography, followed by generation of a velocity-adaptive unstructured tetrahedral mesh (see Methods Section "3D velocity and 3D structural model"); (ii) interpolation of fault slip onto the SeisSol mesh from a given finite fault model; (iii) computing corresponding stress changes in a pseudodynamic relaxation simulation using SeisSol; (iv) generate 120 dynamic rupture simulations varying the 3 dynamic parameters B, C and R; and finally (v) identify a preferred dynamic rupture model from validation using seismic observations (regional waveforms) and the kinematic finite fault model (moment rate function and fault slip distribution).

All models are governed by linear slip-weakening friction [49, 83], with fault friction and stress parameterization fully determined by the 3 parameters, B, C, and R, following [28, 84]. The parameter B serves as a

proportionality factor linking the stress change from the finite-fault model τ_{ffm} and potential stress drop τ_0:

$$\tau_0 = B\tau_{\mathrm{ffm}} + \tau_{\mathrm{d}}\,, \tag{2}$$

τ_{d} is the dynamic strength defined as:

$$\tau_{\mathrm{d}} = \kappa - \mu_{\mathrm{d}} \min(0, \sigma_{\mathrm{n}})\,, \tag{3}$$

with κ ($<$0), the frictional cohesion, σ_{n} the effective normal stress, negative in compression, μ_{d} and the dynamic friction coefficient. We assume that the effective normal stress amplitude $|\sigma_{\mathrm{n}}|$ increases linearly up to 4 km depth and 40 MPa, below which it remains constant (Fig. S12), in line with pore-fluid overpressure observations, predicting a brittle strength approximately constant with depth [31]:

$$\sigma_{\mathrm{n}} = \min(-1 \times 10^6, \max(-40 \times 10^6, 0.4\rho g z))\,. \tag{4}$$

Frictional cohesion amplitude $|\kappa|$ is set constant and equal to 0.25 MPa below 6 km depth, and increases linearly above to 1.25 MPa at 0 km depth (Fig. S12):

$$\kappa(z) = -\kappa_0 - \kappa_1 \max(0, (z + z_{\mathrm{coh}})/z_{\mathrm{coh}})\,, \tag{5}$$

with $z_{\mathrm{coh}} = 6000$ m, κ_0 = 0.25 MPa and κ_1 = 1 MPa.

C acts as a proportionality factor relating the slip weakening distance d_{c} and the fault slip distribution of the reference finite-fault model u_{ffm}. This proportionality is tapered to 15% of the maximum slip magnitude to prevent under-resolved simulations and avoid unrealistic long-distance rupture propagation in regions of low slip:

$$d_{\mathrm{c}} = C \max(0.15 \max(u_{\mathrm{ffm}}), u_{\mathrm{ffm}})\,, \tag{6}$$

Our slip-scaled d_{c} assumption follows the approach of [28], who reported improved waveform fits using a weakening distance proportional to final slip in their dynamic rupture models of the 2015 M_{w}7.8 Nepal earthquake. While uniform d_{c} remains common in dynamic rupture simulations [85, 86] slip-dependent d_{c} may better capture the scale-dependency of fracture energy and dynamic rupture complexity of natural earthquakes [32].

R is the relative prestress ratio (e.g. [29]), which connects the potential stress drop $\tau_0 - \tau_{\mathrm{d}}$ to the frictional strength drop $\tau_{\mathrm{s}} - \tau_{\mathrm{d}}$, as

$$R = (\tau_0 - \tau_{\mathrm{d}})/(\tau_{\mathrm{s}} - \tau_{\mathrm{d}})\,, \tag{7}$$

with τ_0 the initial fault traction, and τ_{s} the static fault strength defined as

$$\tau_{\mathrm{s}} = \kappa - \mu_{\mathrm{s}} \min(0, \sigma_{\mathrm{n}})\,. \tag{8}$$

We use R to constrain τ_{s} (and μ_{s}):

$$\tau_{\mathrm{s}} = \tau_{\mathrm{d}} + (\tau_0 - \tau_{\mathrm{d}})/R\,. \tag{9}$$

We assume a dynamic friction of $\mu_{\rm d} = 0.2$, and enforce $0.22 < \mu_{\rm s} < 1.5$, with $\mu_{\rm s}$ the static friction.

We prescribe a nucleation patch that grows smoothly in time and across a minimal-sized perturbation area, adapted to the friction and stress parameters of each setup, based on Galis et al. [87] estimate. The nucleation center is placed at the on-fault location, nearest to the USGS reviewed hypocenter location (40.374°N 125.022°W, 10km depth)[25] for the dynamic rupture models informed by the kinematic model, and at the same location shifted 2.5km along strike for the geodetically informed dynamic rupture models, because the geodetic model features very little slip near the inferred hypocenter, which challenges nucleation.

We explore all combinations of (B, C, R) with B in $[0.9, 1.0, 1.1]$, C in $[0.1, 0.2, 0.3, 0.4, 0.5]$, and R in $[0.55, 0.6, 0.65, 0.7, 0.75, 0.8, 0.85, 0.9]$, leading to $3 \times 5 \times 8 = 120$ models. The preferred dynamic rupture model informed by the kinematic models is obtained with (B,C,R) = (0.9, 0.2, 0.7). The preferred dynamic rupture model informed by the geodetic model is obtained with (B,C,R) = (1.0, 0.1, 0.6).

Ensemble and best-fitting dynamic rupture models informed from the geodetic slip model

In the main text, we inform the dynamic rupture scenarios by our kinematic model. Alternatively, using the geodetic model to inform dynamic rupture modeling allows discussing velocity structure assumptions and their consequences on earthquake dynamics. Our geodetic model is based on a uniform half-space with G=35 GPa. Since peak slip occurs within the top 5 km, variations in the velocity model significantly impact the modeled earthquake magnitude. To generate more realistic ground motions synthetics, we use a 1D velocity structure in dynamic rupture models informed by the geodetic model, rather than a homogeneous half-space. We select the stiffer 1D velocity model from LITHO1.0, also used in the USGS inversion, as it produces $M_{\rm w}7$ earthquake scenarios. In contrast, the 1D velocity model used in the kinematic inversion results in $M_{\rm w}6.8$ scenarios. The preferred dynamic rupture scenario, obtained with (B,C,R)=(1.0,0.1,0.6), is shown in Fig. S15. Our preferred dynamic rupture scenario informed by the geodetic model is in overall agreement with the preferred dynamic rupture scenario informed by the kinematic model. Rupture is predominantly unilateral to the west, with a smooth slip distribution that deepens in that direction and peaks at shallow depths. The geodetic slip distribution poses a challenge for rupture nucleation due to limited slip in the hypocentral region, requiring the hypocenter to be placed 2.5 km farther east than inferred. A localized supershear transition occurs at the eastern edge of the main slip patch. The model has overall 24% of its rupture area at supershear rupture speed. Notably, a deeper region of low slip is dynamically connected to the main rupture asperity, and corresponds with the deep and isolated asperities to the east in the preferred dynamic rupture scenario based on the kinematic model.

Dynamic and static Coulomb stress modeling

We compute the static and peak dynamic Coulomb failure stress change (ΔCFS) [20] on the Cascadia subduction interface and the San Andreas Fault from the 3D dynamic rupture simulations of the preferred model. The Coulomb failure stress change is given by:

$$\Delta\text{CFS} = \Delta\tau - \mu_{\rm s}\Delta\sigma_{\rm n}\,, \tag{10}$$

where $\Delta\tau$ and $\Delta\sigma_{\mathrm{n}}$ are the shear and normal stress changes on the fault, respectively, and μ_{s} = 0.6 is the static friction coefficient. We evaluate $\Delta\tau$ in the expected direction of maximum tectonic loading: along-dip in the direction of reverse-sense motion for Cascadia, and along-strike in the direction of right-lateral strike-slip motion for the San Andreas Fault.

Supplementary Animations

We provide three animations illustrating the kinematic and preferred dynamic models at `https://syncandshare.lrz.de/getlink/fi2AacRuynwAVF2rasXVy7/`.

- **Animation 1:** `Mendocino_kinematic_model_interpolated_slip_rate.mp4` - Rupture evolution in the kinematic model (Fig. 2), shown as absolute slip rate (m/s). The model comprises 240 subfaults (Fig. 2b) and is interpolated for visualization purposes.
- **Animation 2:** `Mendocino_DR_from_kinematic_model_slip_rate.mp4` — Rupture dynamics of the preferred 3D dynamic rupture scenario (Fig. 3), shown as absolute slip rate (m/s).
- **Animation 3:** `Mendocino_wavefield_vertical_velocity.mp4` — Simulated vertical velocity wavefield (m/s) at the free surface accounting for topography and bathymetry, illustrating rupture directivity and the influence of the 3D velocity structure.
- **Animation 4:** `Mendocino_DR_from_geodetic_model_slip_rate.mp4` — Rupture dynamics of the 3D dynamic rupture scenario informed by the geodetic model (Fig. S15), shown as absolute slip rate (m/s).

References

15. Goldberg, D. E., Koch, P., Melgar, D., Riquelme, S. & Yeck, W. L. Beyond the Teleseism: Introducing Regional Seismic and Geodetic Data into Routine USGS Finite-Fault Modeling. *Seismological Research Letters* **93,** 3308–3323. doi:10.1785/0220220047 (2022).

20. Jia, Z. *et al.* The complex dynamics of the 2023 Kahramanmaraş, Turkey, ¡i¿M¡/i¿¡sub¿w¡/sub¿ 7.8-7.7 earthquake doublet. *Science* **381,** 985–990. doi:10.1126/science.adi0685 (2023).

23. Magen, Y. *et al.* Fault coalescence, slip distribution, and stress drop of the February 2023 southeast Türkiye earthquakes from joint inversion of SAR, GNSS, and burst overlap interferometry. *Seismological Research Letters* **95,** 680–696 (2024).

24. Lomax, A. *NLL-SSST-coherence High-Precision Earthquake Location Catalog for the M 7.0, 2024 Offshore Cape Mendocino, California Earthquake Sequence* 2025. doi:10.5281/zenodo.14588299.

25. USGS. 2024. https://earthquake.usgs.gov/earthquakes/eventpage/nc75095651/origin/detail.

26. Stephenson, W. J., Reitman, N. G. & Angster, S. J. *P-and S-wave velocity models incorporating the Cascadia subduction zone for 3D earthquake ground motion simulations, Version 1.6—Update for Open-File Report 2007–1348* tech. rep. (US Geological Survey, 2017). doi:10.3133/ofr20171152.

27. Pasyanos, M. E., Masters, T. G., Laske, G. & Ma, Z. LITHO1.0: An Updated Crust and Lithospheric Model of the Earth. *Journal of Geophysical Research: Solid Earth* **119,** 2153–2173. doi:10.1002/2013JB010626 (2014).

28. Weng, H. & Yang, H. Constraining frictional properties on fault by dynamic rupture simulations and near-field observations. *Journal of Geophysical Research: Solid Earth* **123,** 6658–6670 (2018).

29. Aochi, H. & Madariaga, R. The 1999 İzmit, Turkey, Earthquake: Nonplanar Fault Structure, Dynamic Rupture Process, and Strong Ground Motion. *Bulletin of the Seismological Society of America* **93,** 1249–1266. doi:10.1785/0120020167 (2003).

31. Suppe, J. Fluid Overpressures and Strength of the Sedimentary Upper Crust. *Journal of Structural Geology* **69,** 481–492. doi:10.1016/j.jsg.2014.07.009 (2014).

32. Gabriel, A.-A., Garagash, D. I., Palgunadi, K. H. & Mai, P. M. Fault Size–Dependent Fracture Energy Explains Multiscale Seismicity and Cascading Earthquakes. *Science* **385,** eadj9587. doi:10.1126/science.adj9587 (2024).

36. Williamson, A., Lux, A. & Allen, R. M. Performance of bEPIC Through the 2024 M 7.0 Mendocino Earthquake Sequence. *The Seismic Record* **5,** 127–135. doi:10.1785/0320250009 (2025).

49. Andrews, D. Rupture propagation with finite stress in antiplane strain. *Journal of Geophysical Research* **81,** 3575–3582 (1976).

56. Ulrich, T. & Gabriel, A.-A. *Rapid, Automatized 3D Dynamic Rupture Simulations for the Physics-Based Characterization of Large Earthquakes* 2024. doi:10.5281/zenodo.15188183.

57. Lomax, A. & Savvaidis, A. High-Precision Earthquake Location Using Source-Specific Station Terms and Inter-Event Waveform Similarity. *Journal of Geophysical Research: Solid Earth* **127.** e2021JB023190 2021JB023190, e2021JB023190. doi:https://doi.org/10.1029/2021JB023190. eprint: https://agupubs.onlinelibrary.wiley.com/doi/pdf/10.1029/2021JB023190 (2022).

59. Lomax, A. & Henry, P. Major California faults are smooth across multiple scales at seismogenic depth. *Seismica* **2.** doi:10.26443/seismica.v2i1.324 (2023).

60. Lomax, A., Tuvè, T., Giampiccolo, E. & Cocina, O. A new view of seismicity under Mt. Etna volcano, Italy, 2014-2023 from multi-scale high-precision earthquake relocations. *Annals of Geophysics* **67,** S437–S437 (2024).

61. Okada, Y. Internal deformation due to shear and tensile faults in a half-space. *Bulletin of the seismological society of America* **82,** 1018–1040 (1992).

62. Lawson, C. L. & Hanson, R. J. Linear least squares with linear inequality constraints. *Solving least squares problems,* 158–173 (1974).

63. Koch, P., Bravo, F., Riquelme, S. & Crempien, J. G. F. Near-Real-Time Finite-Fault Inversions for Large Earthquakes in Chile Using Strong-Motion Data. *Seismological Research Letters* **90,** 1971–1986. doi:10.1785/0220180294 (2019).

64. Ji, C., Wald, D. J. & Helmberger, D. V. Source Description of the 1999 Hector Mine, California, Earthquake, Part I: Wavelet Domain Inversion Theory and Resolution Analysis. *Bulletin of the Seismological Society of America* **92,** 1192–1207. doi:10.1785/0120000916 (2002).

65. US Geological Survey, E. H. P. Advanced National Seismic System (ANSS) comprehensive catalog of earthquake events and products: Various (2017).

66. Dziewonski, A. M. & Anderson, D. L. Preliminary reference Earth model. *Physics of the earth and planetary interiors* **25,** 297–356. doi:10.1016/0031-9201(81)90046-7 (1981).

67. Graves, R. Rupture history and strong ground motion modeling of the 1992 Cape Mendocino earthquake. *Report to USGS, award* (1994).

68. Kennett, B. L. N. & Engdahl, E. R. Traveltimes for global earthquake location and phase identification. *Geophys. J. Int.* **105,** 429–465. doi:https://doi.org/10.1111/j.1365-246X.1991.tb06724.x (1991).

69. Ishii, M., Shearer, P. M., Houston, H. & Vidale, J. E. Extent, duration and speed of the 2004 Sumatra–Andaman earthquake imaged by the Hi-Net array. *Nature* **435,** 933–936 (2005).

70. Kiser, E. & Ishii, M. Back-projection imaging of earthquakes. *Annual Review of Earth and Planetary Sciences* **45,** 271–299 (2017).

71. Ghosh, A., Vidale, J. E. & Creager, K. C. Tremor asperities in the transition zone control evolution of slow earthquakes. *J. Geophys. Res. Solid Earth* **117,** B10301. doi:https://doi.org/10.1029/2012JB009249 (2012).

72. Dumbser, M. & Käser, M. An arbitrary high-order discontinuous Galerkin method for elastic waves on unstructured meshes—II. The three-dimensional isotropic case. *Geophysical Journal International* **167,** 319–336. doi:10.1111/j.1365-246X.2006.03120.x (2006).

73. Breuer, A. *et al.* in *Supercomputing. ISC 2014. Lecture Notes in Computer Science, vol 8488* 1–18 (Springer, 2014). doi:10.1007/978-3-319-07518-1_1.

74. Heinecke, A. *et al. Petascale high order dynamic rupture earthquake simulations on heterogeneous supercomputers* in *SC'14: International Conference for High-Performance Computing, Networking, Storage and Analysis* (2014). doi:doi.org/10.1109/SC.2014.6.

75. Rettenberger, S., Meister, O., Bader, M. & Gabriel, A.-A. *ASAGI: A Parallel Server for Adaptive Geoinformation* in *Proceedings of the Exascale applications and Software Conference 2016* (ACM, Stockholm, Sweden, 2016), 2:1–2:9. doi:10.1145/2938615.2938618.

76. Uphoff, C. *et al. Extreme scale multi-physics simulations of the tsunamigenic 2004 Sumatra megathrust earthquake* in *Proceedings of the International Conference for High Performance Computing, networking, Storage and Analysis, SC 2017* (2017). doi:10.1145/3126908.3126948.

77. Krenz, L. *et al. 3D acoustic-elastic coupling with gravity: the dynamics of the 2018 Palu, Sulawesi earthquake and tsunami* in *Proceedings of the International Conference for High-Performance Computing, Networking, Storage and Analysis* (ACM, St. Louis, Missouri, 2021). doi:10.1145/3458817.3476173.

747 78. Pelties, C., Gabriel, A.-A. & Ampuero, J.-P. Verification of an ADER-DG method for complex dynamic
748 rupture problems. *Geoscientific Model Development* **7,** 847–866. doi:10.5194/gmd-7-847-2014
749 (2014).

750 79. Harris, R. A. *et al.* A suite of exercises for verifying dynamic earthquake rupture codes. *Seismol. Res. Lett.*
751 **89,** 1146–1162. doi:10.1785/0220170222 (2018).

752 80. Wollherr, S., Gabriel, A.-A. & Uphoff, C. Off-fault plasticity in three-dimensional dynamic rupture simula-
753 tions using a modal Discontinuous Galerkin method on unstructured meshes: Implementation, verification
754 and application. *Geophys. J. Int.* **214,** 1556–1584. doi:10.1093/gji/ggy213 (2018).

755 81. Kristeková, M., Kristek, J., Moczo, P. & Day, S. M. Misfit Criteria for Quantitative Comparison of Seis-
756 mograms. *Bulletin of the Seismological Society of America* **96,** 1836–1850. doi:10.1785/0120060012
757 (2006).

758 82. Kristeková, M., Kristek, J. & Moczo, P. Time-Frequency Misfit and Goodness-of-Fit Criteria for Quantitative
759 Comparison of Time Signals. *Geophysical Journal International* **178,** 813–825. doi:10.1111/j.1365-
760 246X.2009.04177.x (2009).

761 83. Ida, Y. Cohesive force across the tip of a longitudinal-shear crack and Griffith's specific surface energy.
762 *Journal of Geophysical Research* **77,** 3796–3805 (1972).

763 84. Tinti, E. *et al.* Constraining Families of Dynamic Models Using Geological, Geodetic and Strong Ground
764 Motion Data: The Mw 6.5, October 30th, 2016, Norcia Earthquake, Italy. *Earth and Planetary Science Letters*
765 **576,** 117237. doi:10.1016/j.epsl.2021.117237 (2021).

766 85. Ma, S. A physical model for widespread near-surface and fault zone damage induced by earthquakes. en.
767 *Geochemistry, Geophysics, Geosystems* **9.** doi:10.1029/2008GC002231 (2008).

768 86. Douilly, R., Aochi, H., Calais, E. & Freed, A. M. Three-Dimensional Dynamic Rupture Simulations across
769 Interacting Faults: The Mw7.0, 2010, Haiti Earthquake. *Journal of Geophysical Research: Solid Earth* **120,**
770 1108–1128. doi:10.1002/2014JB011595 (2015).

771 87. Galis, M. *et al.* On the Initiation of Sustained Slip-Weakening Ruptures by Localized Stresses. *Geophysical*
772 *Journal International* **200,** 890–909. doi:10.1093/gji/ggu436 (2015).

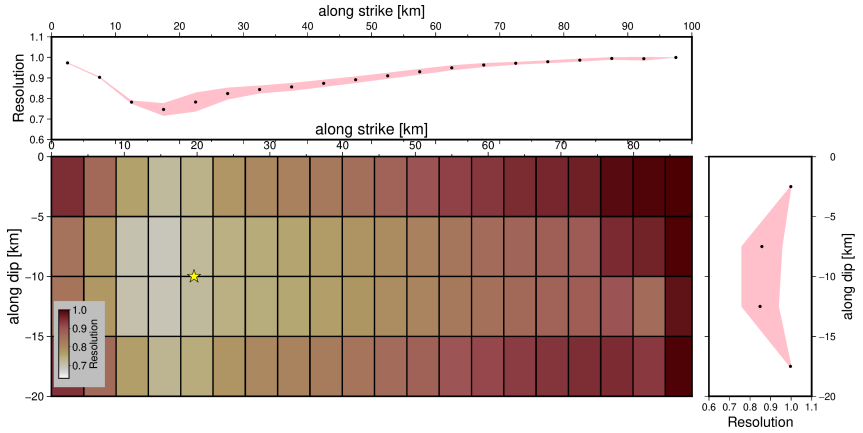

Figure S1: Empirical geodetic model resolution test. The sensitivity of the inversion scheme to slip along each of the model subfaults is represented by the resolution, which is the correlation between the inverted slip distribution and synthetic slip distribution along the ith subfault. This test involves calculating GNSS displacement due to a synthetic slip distribution, adding noise based on GNSS uncertainties, inverting for the slip distribution from the noisy data, and computing the correlation between the synthetic and inverted slip distributions.

Type	Reference	LITHO1.0	With Cascadia
GNSS	0.045	0.047	0.051
HNE	0.044	0.053	0.039
HNN	0.043	0.052	0.041
HNZ	0.057	0.066	0.051
L	0.009	0.009	0.009
P	0.067	0.077	0.049
R	0.023	0.023	0.020
SH	0.040	0.041	0.040
Total	0.328	0.367	0.299

Table S1: Decomposition of the misfit by data type for three kinematic models: (1) the reference model based on a 1D crustal velocity structure from CCVMv1.6, (2) an alternative model using the routinely derived crustal velocity model from WASP based on LITHO1.0, and (3) a two-fault kinematic model incorporating the Cascadia subduction interface. Data types include strong-motion records in the east-west (HNE), north-south (HNN), and vertical (HNZ) components, body P and SH waves, surface Love (L) and Rayleigh (R) waves, and static GNSS measurements.

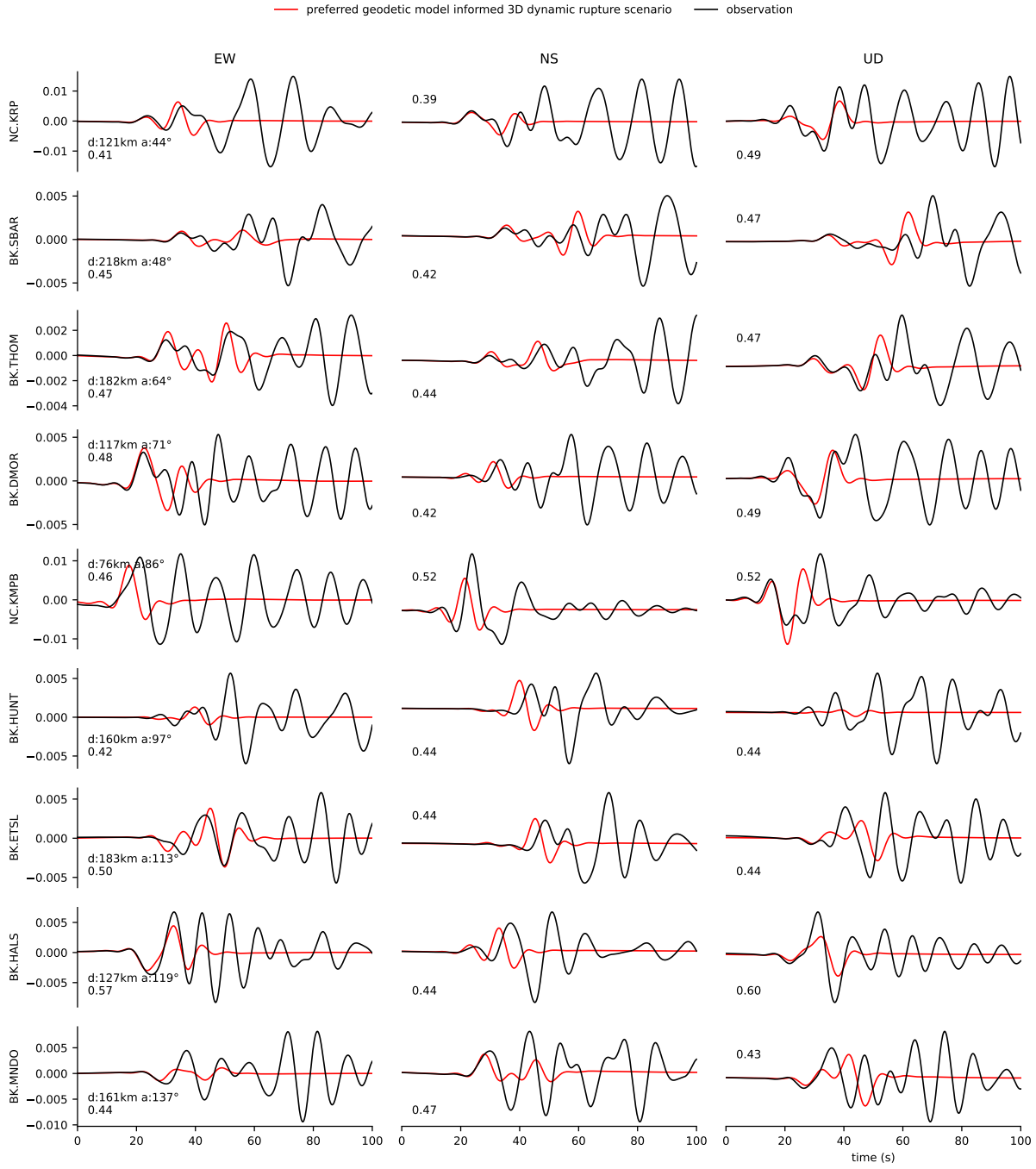

Figure S2: Velocity waveform comparison at selected strong-motion stations for the preferred geodetic model informed 3D dynamic rupture scenario, (Fig. S15). Observed waveforms are plotted in black. All waveforms are band-pass filtered between 0.016 Hz and 0.25 Hz. The station location is plotted in Fig. S13. Annotations provide for each station, distance, and azimuth relative to the hypocenter (first line), and goodness of fit (second) line.

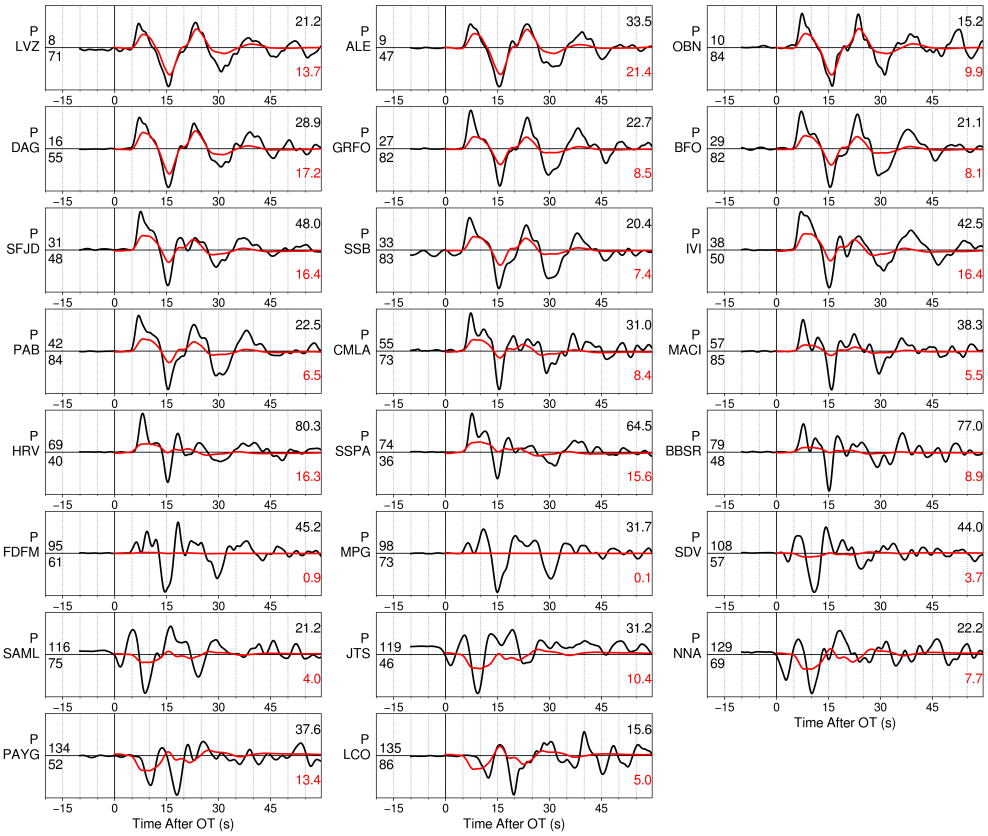

Figure S3: Comparison of synthetic (red) and observed (black) teleseismic displacement waveforms from the kinematic model during the P-wave time window. A 1–170 s band-pass filter is applied to all traces.

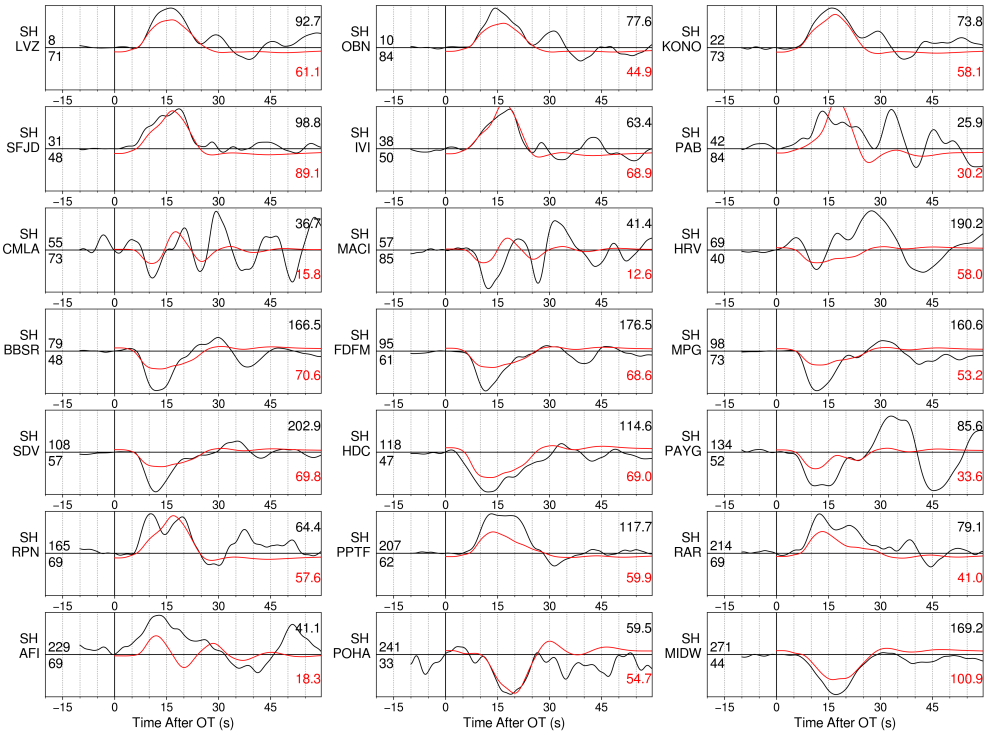

Figure S4: Comparison of synthetic (red) and observed (black) teleseismic displacement waveforms from the kinematic model during the SH-wave time window. A 1–170 s band-pass filter is applied to all traces.

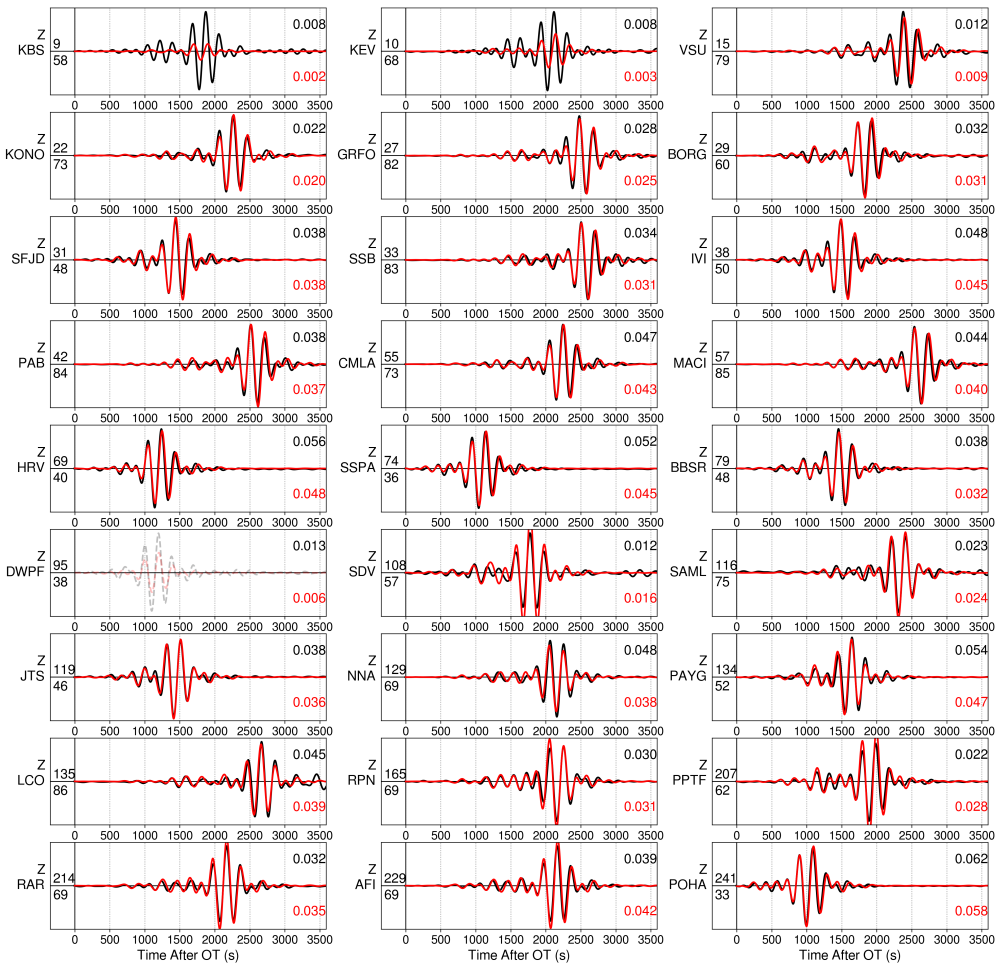

Figure S5: Comparison of synthetic (red) and observed (black) teleseismic Rayleigh surface waveforms from the kinematic model, in displacement. A 1–170 s band-pass filter is applied to all traces.

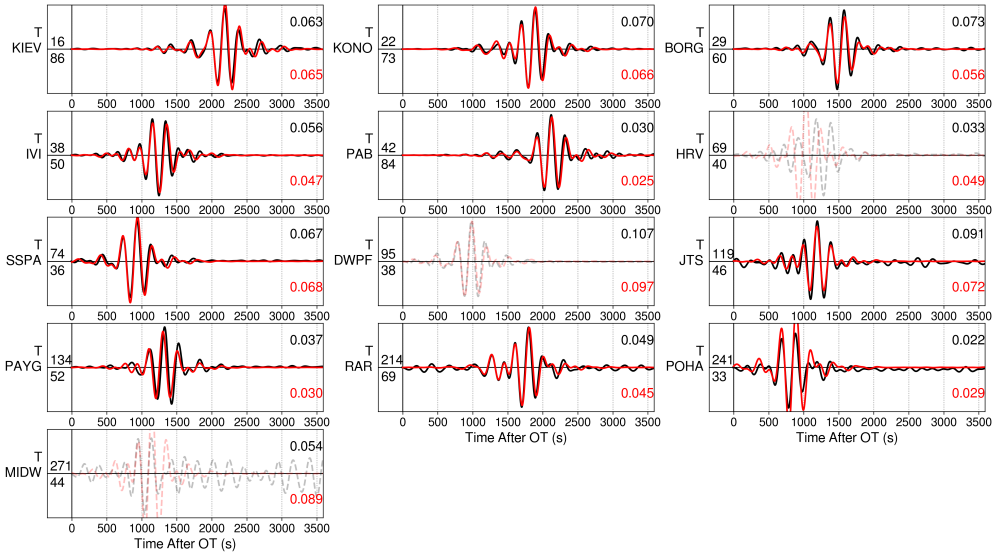

Figure S6: Comparison of synthetic (red) and observed (black) teleseismic Love surface waveforms from the kinematic model, in displacement. A 1–170 s band-pass filter is applied to all traces.

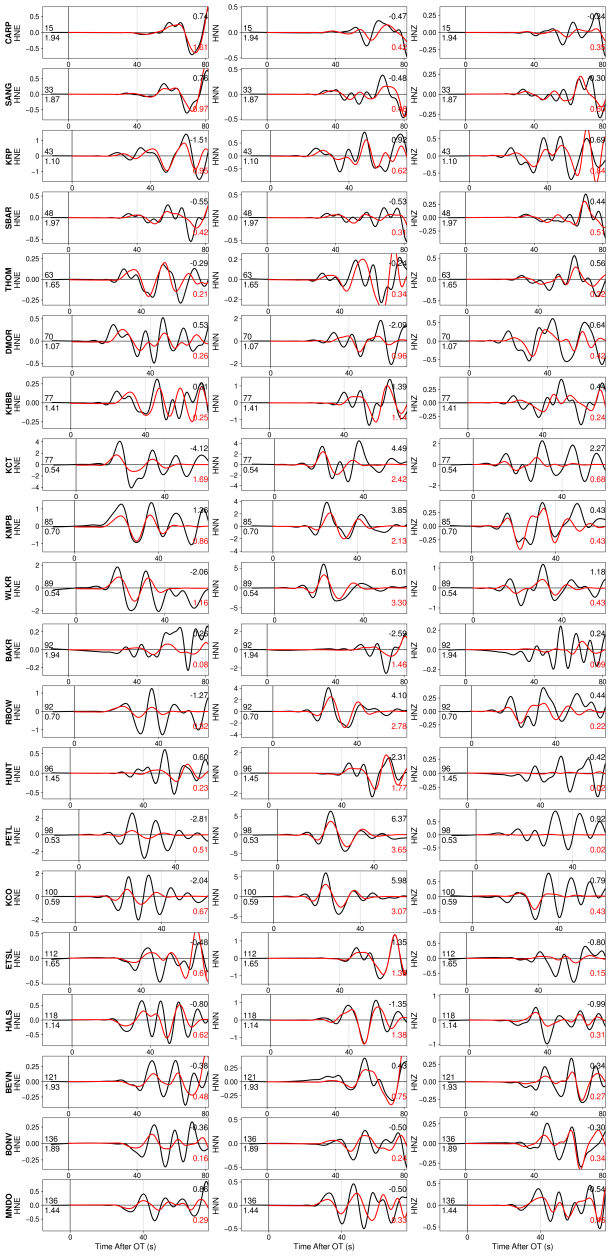

Figure S7: Comparison of synthetic (red) and observed (black) regional velocity waveforms from the kinematic model. An 8-100 s band-pass filter is applied to all traces.

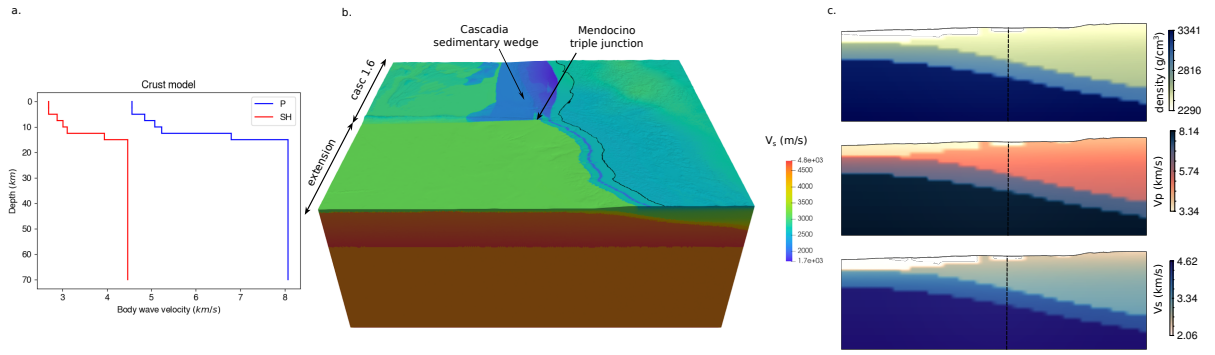

Figure S8: (a.) P and S wave velocity in the assumed depth-dependent crustal velocity model extracted from the Cascadia velocity model v1.6 ([26], CCVMv1.6) at (-124.75°, 40.5°), used in our kinematic inversion. (b.) 3D crustal velocity model evaluated on our 3D mesh, extended to the South from CCVMv1.6, used in our dynamic rupture simulations informed by the kinematic model. (c.) 3D crustal velocity model (from top to bottom, density, P- and S-wave velocity) evaluated on the Mendocino fault. The x-location where we evaluate the 1D velocity model from the 3D velocity model is marked by a dashed line. Our 1D velocity model is evaluated from a coarsely sampled (2.5 km vs 1 km) model.

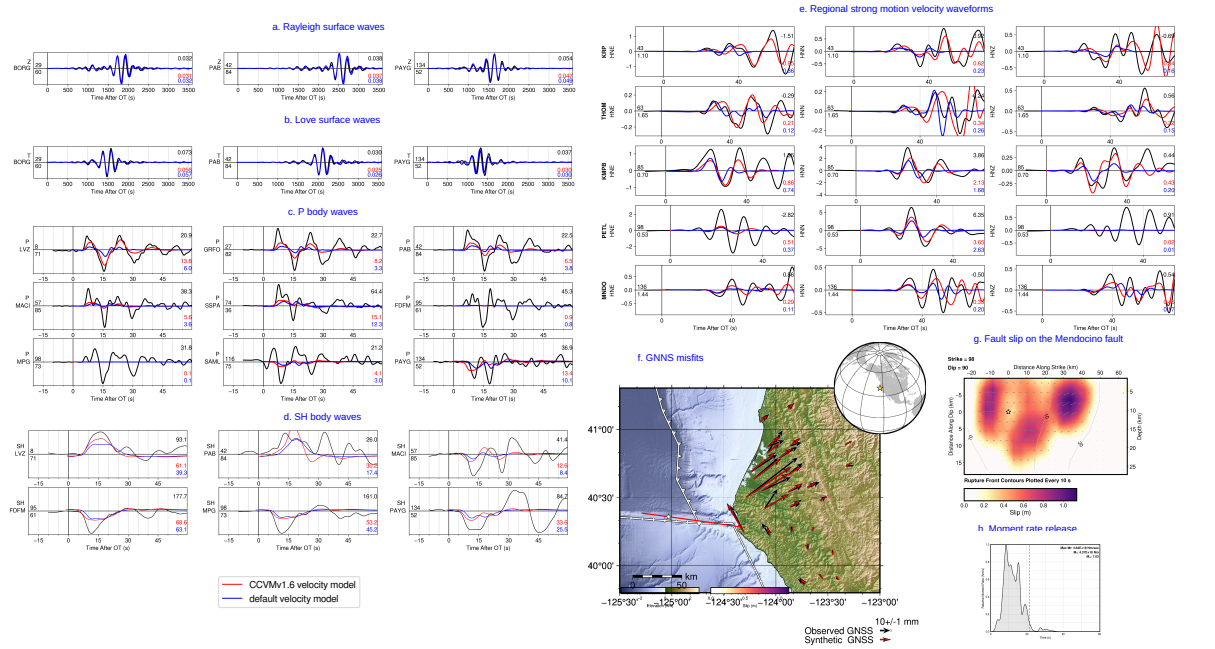

Figure S9: Sensitivity of the kinematic fault inversion to the choice of a 1D crustal velocity structure. Fit to selected surface Rayleigh (a.) and Love (b.) waves, P (c.) and SH (d.) body waves, regional waveforms (e.), and GNSS (f.) data. The fault slip on the Mendocino fault is plotted in (g.) and the moment rate function is given in (h.).

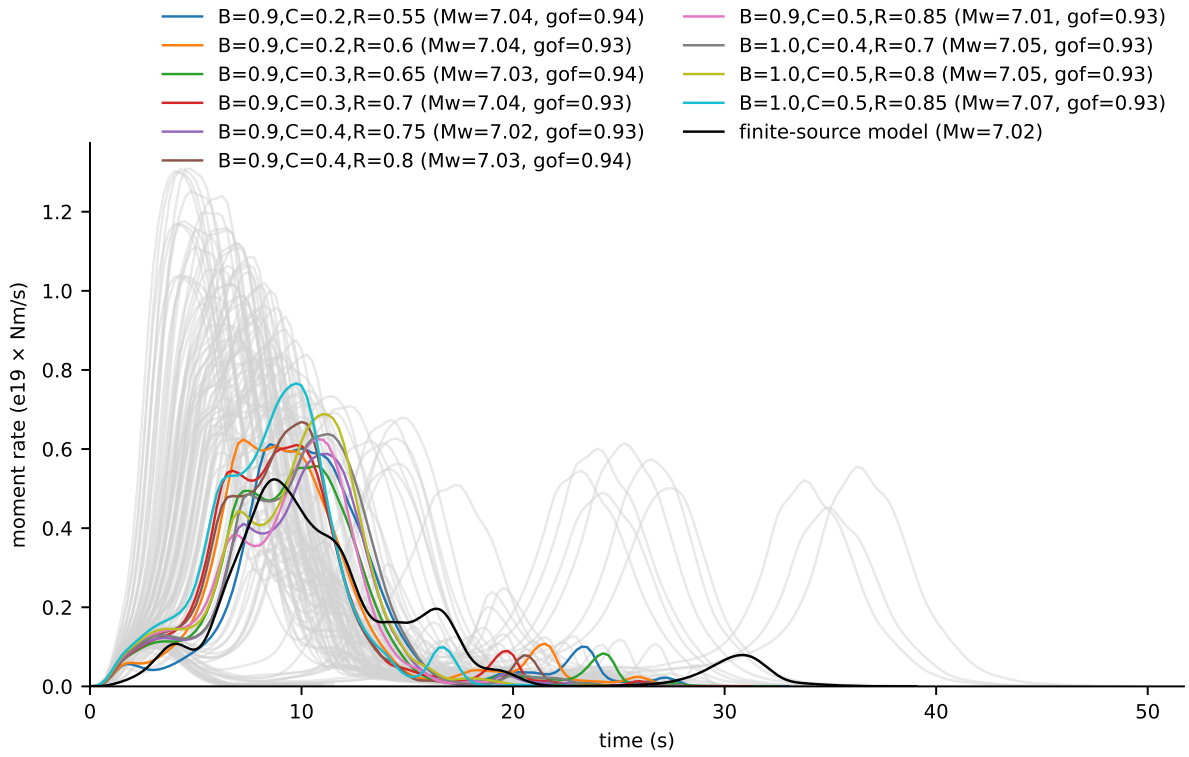

Figure S10: Moment rate functions for 3D dynamic rupture scenarios informed by our kinematic model, forming an ensemble of 120 different dynamic rupture models, compared with the moment rate function of the kinematic model itself (black line). The 10 dynamic rupture models best fitting the moment rate function of the kinematic model are shown with colored lines, while the remaining models are shown with grey lines.

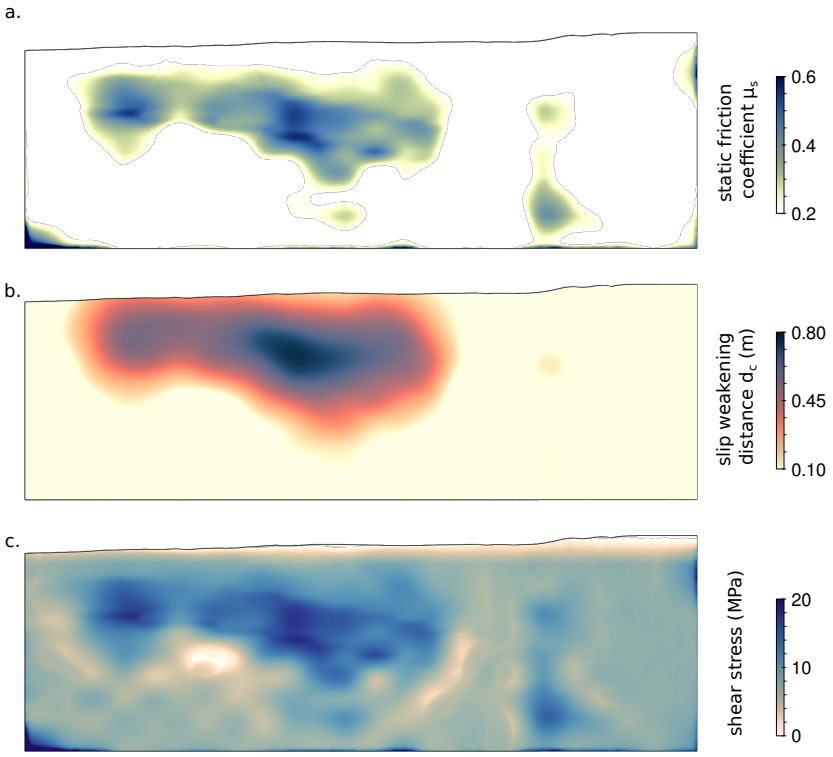

Figure S11: dynamic rupture parameters in the preferred 3D dynamic rupture scenario, informed from our kinematic model, with parameters (B, C, R) = (0.9, 0.3, 0.7). (a.) static friction coefficient μ_{s}. (b.) linear slip weakening distance d_{c} in m. (c.) Initial shear stress in MPa.

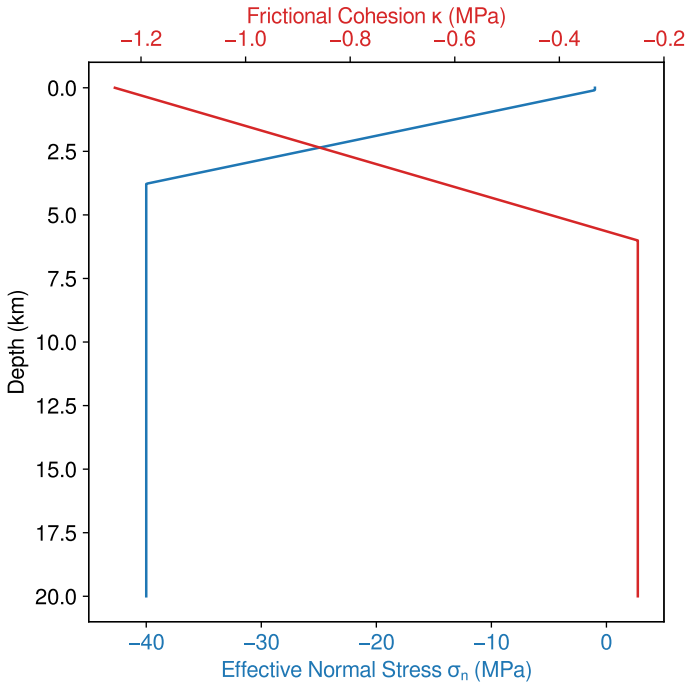

Figure S12: Depth dependence of effective normal stress σ_{n} (blue) and frictional cohesion κ (red).

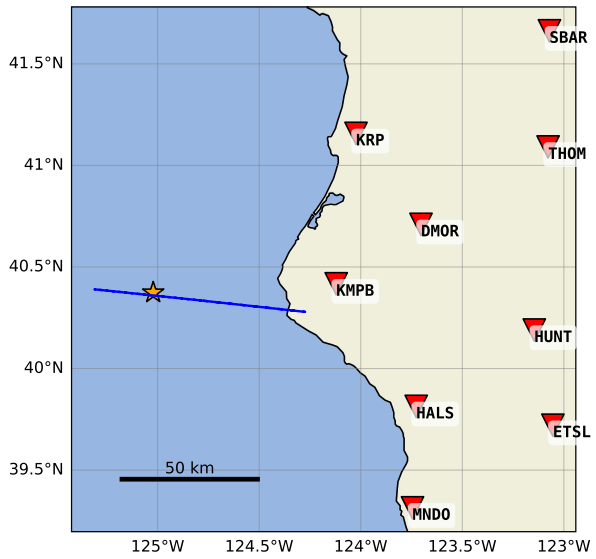

Figure S13: Map of selected strong-motion stations used to evaluate the fit to observations from the ensemble of dynamic rupture scenarios. The hypocenter is marked with a star, and the fault plane considered in the inversion is shown in blue.

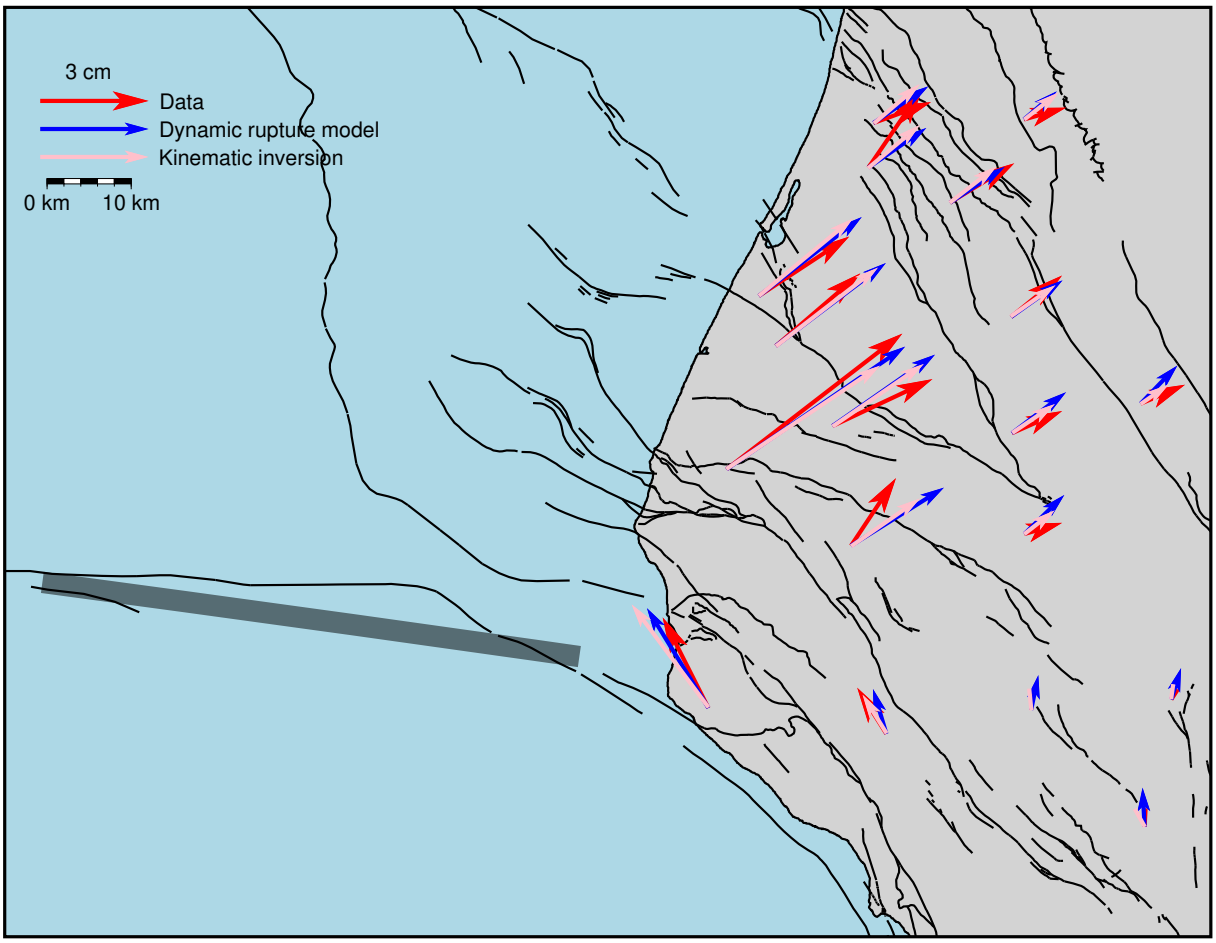

Figure S14: Horizontal co-seismic surface deformation. Blue and pink vectors represent the modeled horizontal displacements from the preferred dynamic rupture model, informed by the kinematic finite-fault model, and from the kinematic finite-fault model itself, respectively. Red vectors show Nevada Geodetic Laboratory processed data [55]. The figure also includes known fault traces [50], and the fault slip region from our kinematic finite-fault model (shaded area).

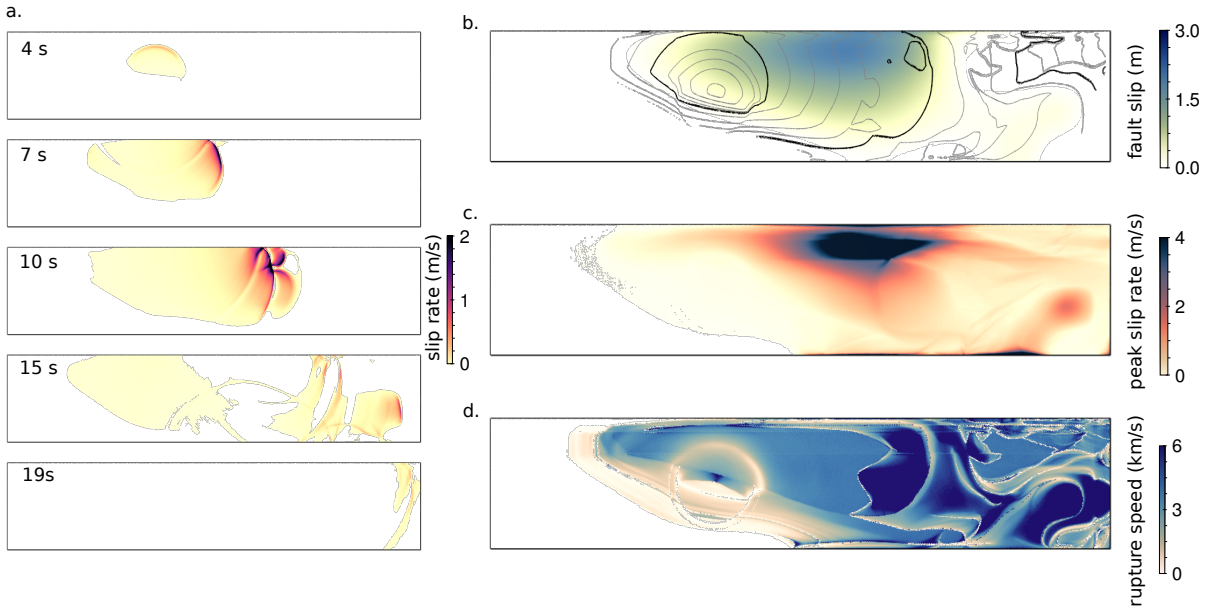

Figure S15: Preferred geodetic model informed 3D dynamic rupture scenario. (a.) Snapshots of absolute slip rate (see also Animation 4). (b.) Total fault slip in m, and rupture time contours every s (grey) and 5 s (black). (c.) Peak slip rate in m/s. (d.) Rupture rupture speed in km/s.

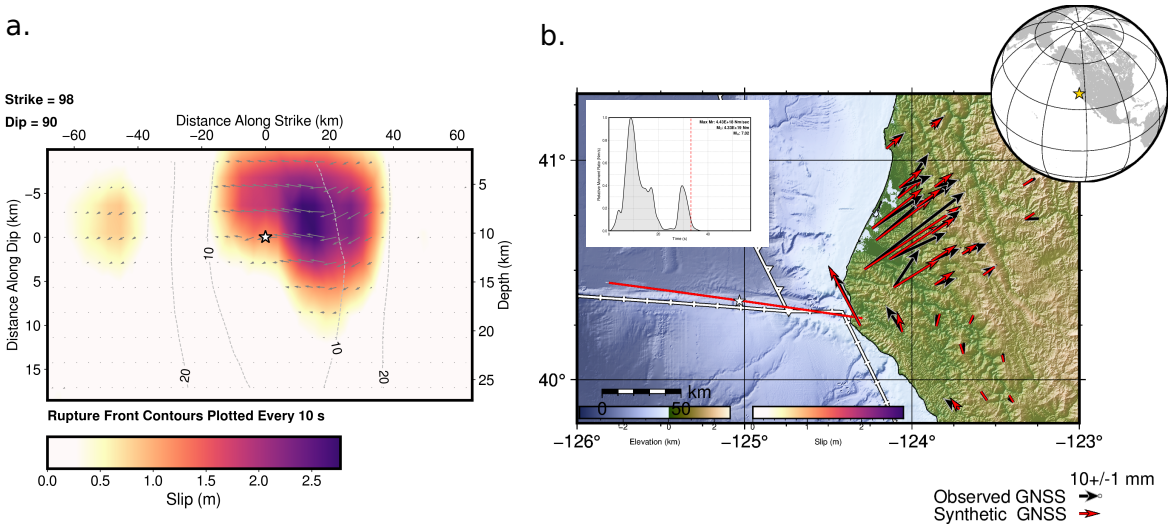

Figure S16: Finite fault model obtained by extending the fault 50 km further west. (a.) Fault slip distribution, showing a secondary slip 40–60 km west of the hypocenter, separated by a 20 km gap from the main slip region. (b.) Fault trace and fit to static GNSS data. The moment rate function is plotted in the inset.

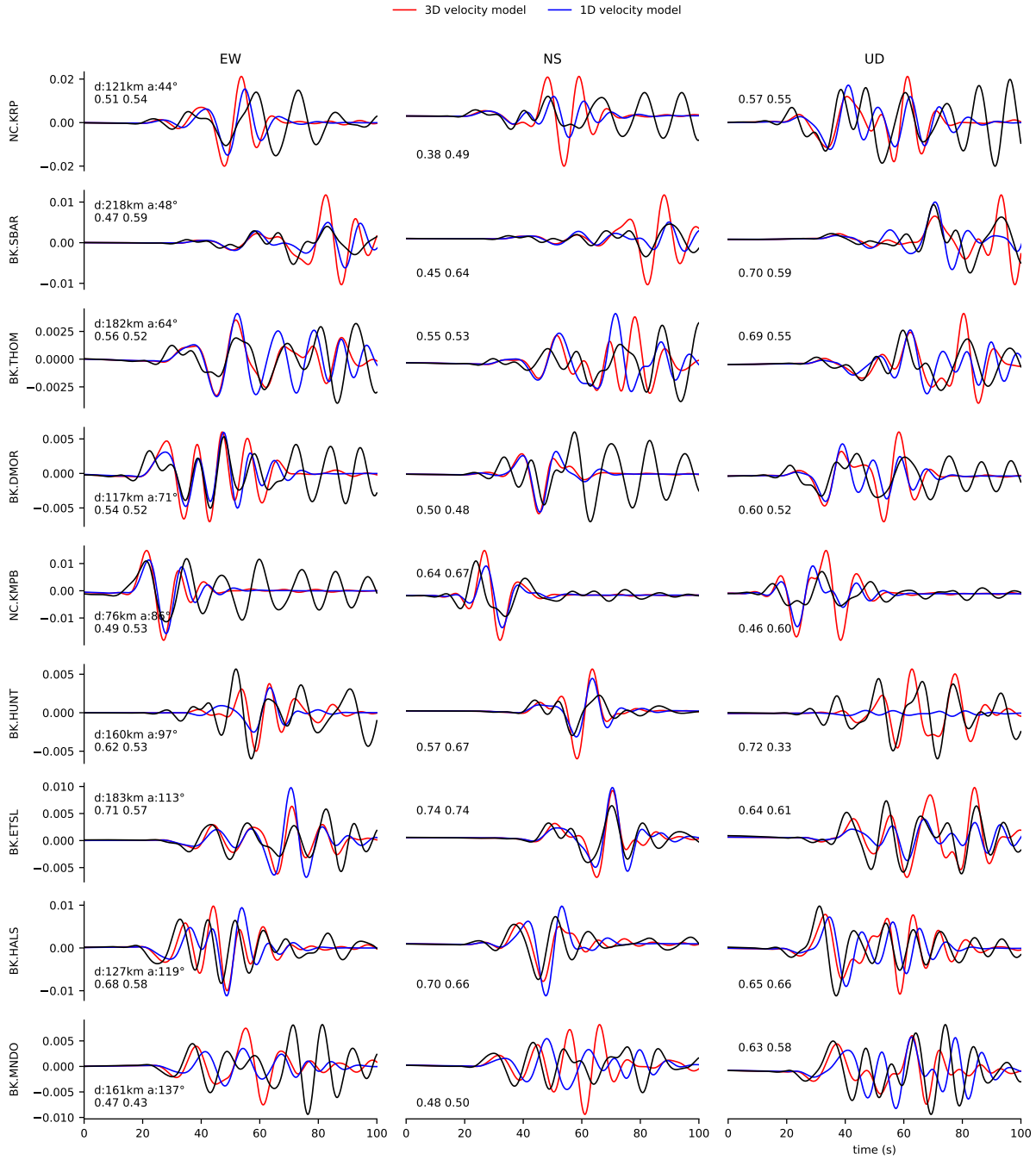

Figure S17: Velocity waveform comparison at selected strong-motion stations for the preferred dynamic rupture model, informed from the kinematic model and incorporating a 3D velocity model (red, Fig. S8b, Methods Sec. "3D velocity and 3D structural model") and for a corresponding multi-point source model and a 1D velocity model, using the Axitra software (blue, Fig. S8a). All waveforms are band-pass filtered between 0.016 and 0.25Hz. The station location is plotted in Fig. S13. Annotations provide for each station, distance, and azimuth relative to the hypocenter (first line), and goodness of fit (second) line, for waveforms based on the 3D and the 1D velocity structure, respectively.

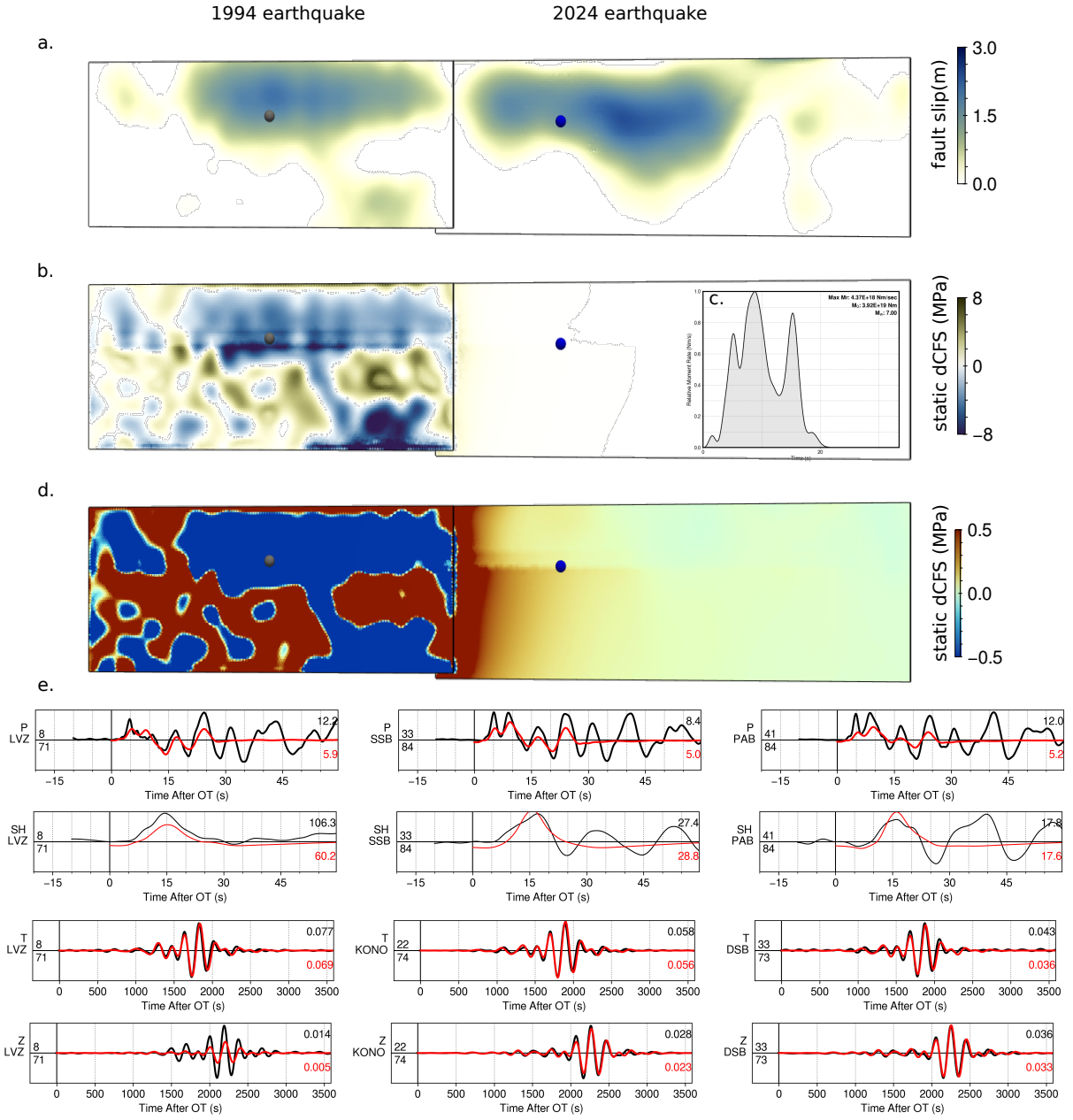

Figure S18: (a.) Fault slip of the M_{w}7.0 1994 earthquake on the Mendocino Transform Fault (left), adjacent to the fault slip of the M_{w}7.0 2024 earthquake (right). Colored spheres indicate the hypocenters of both events. (b.) Static Coulomb stress change imparted by the 1994 earthquake. (c.) Moment rate function of the 1994 earthquake. (d.) Same as (b), but using a saturated color scale to better highlight the positive Coulomb stress change in the hypocentral region of the 2024 event. (e.) Fit to selected P, SH body waves, and surface Love and Rayleigh waves (top to bottom rows).

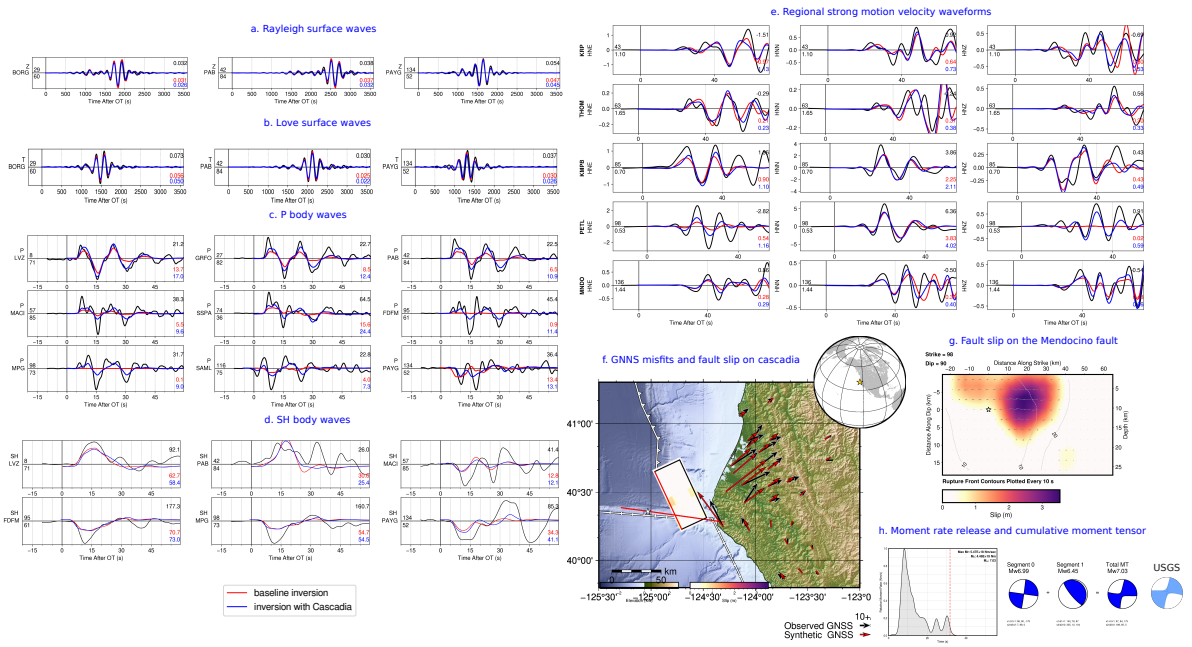

Figure S19: Two faults finite fault model with the Cascadia subduction interface. Fit to selected surface Rayleigh (a.) and Love (b.) waves, P (c.) and SH (d.) body waves, regional waveforms (e.), and GNSS (f.) data. The fault slip on Cascadia is plotted in (f.), and in (g.) for the Mendocino fault. The moment rate function is given in (h.), as well as the inferred moment tensor representation, compared with the inferred moment tensor from the USGS catalog.

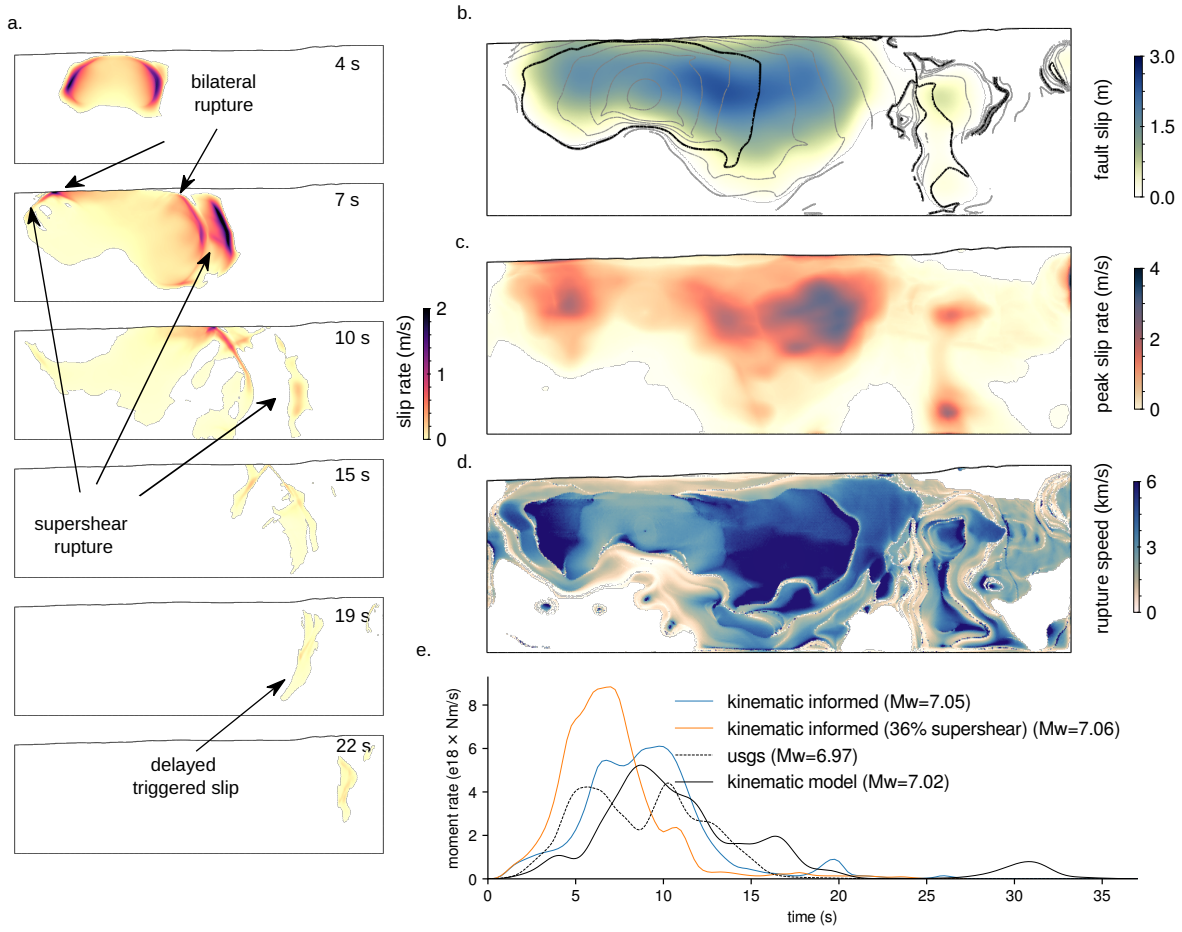

Figure S20: Alternative 3D dynamic rupture scenario, informed from our kinematic model, with a higher proportion of supershear rupture speed, obtained with parameters (B,C,R) = (0.9,0.2,0.8). (a.) Snapshots of absolute slip rate. (b.) Total fault slip in m, and rupture time contours every s (grey) and 5 s (black). (c.) Peak slip rate in m/s. (d.) Rupture rupture speed in m/s. (e.) Moment rate function of the preferred and alternative dynamic rupture scenario compared to our kinematic model, and the USGS kinematic model [15].

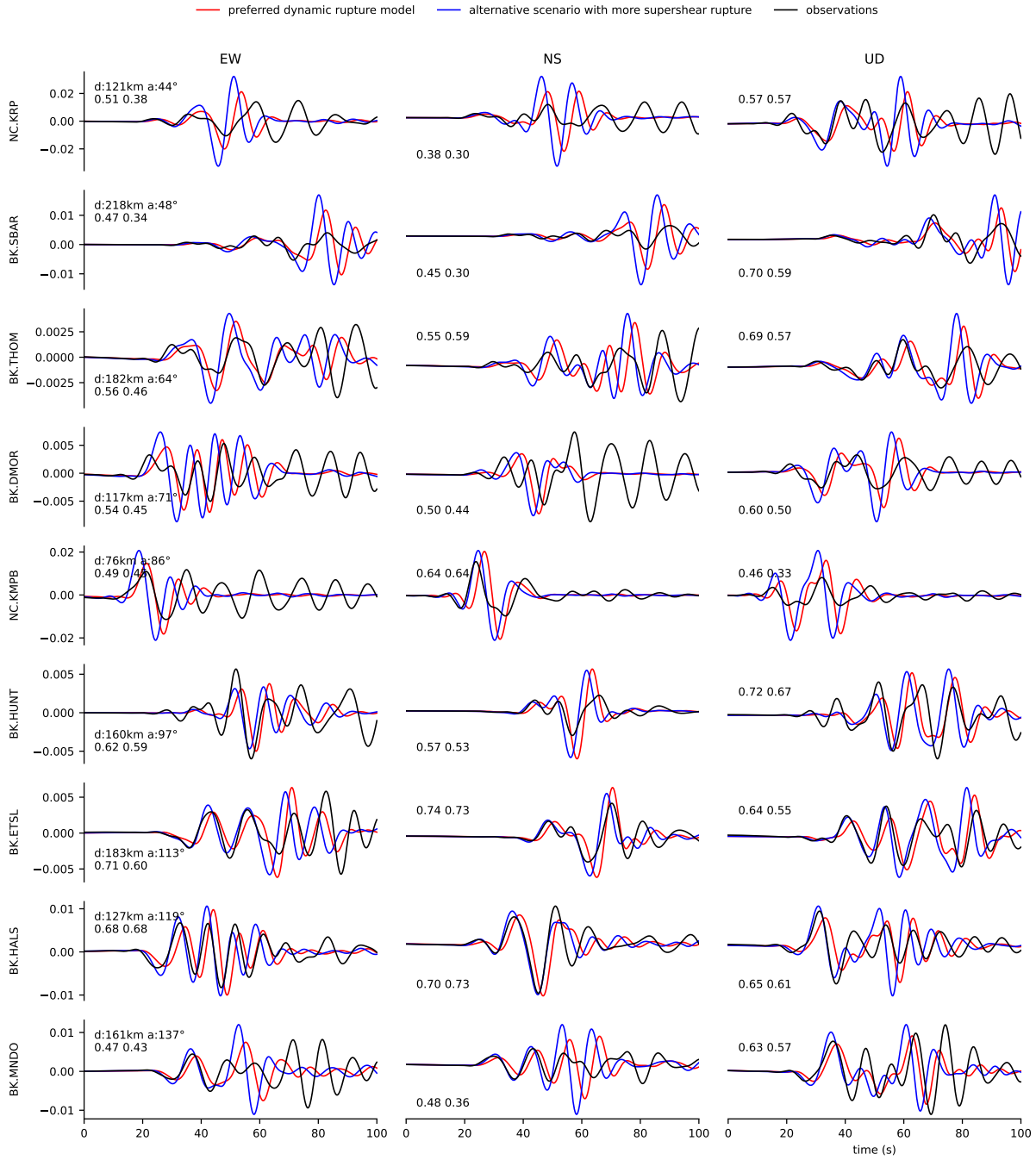

Figure S21: Velocity waveform comparison at selected strong-motion stations for the preferred model (red, 16% of rupture area at supershear rupture speed) and an alternative 3D dynamic rupture scenario (blue, 36% supershear, Fig. S20), informed by our kinematic model with parameters (B,C,R) = (0.9,0.2,0.8). Observed waveforms are plotted in black. All waveforms are band-pass filtered between 0.016 Hz and 0.25 Hz. The station location is plotted in Fig. S13. Annotations provide for each station, distance, and azimuth relative to the hypocenter (first line), and goodness of fit (second) line, for the preferred and alternative dynamic models, respectively.

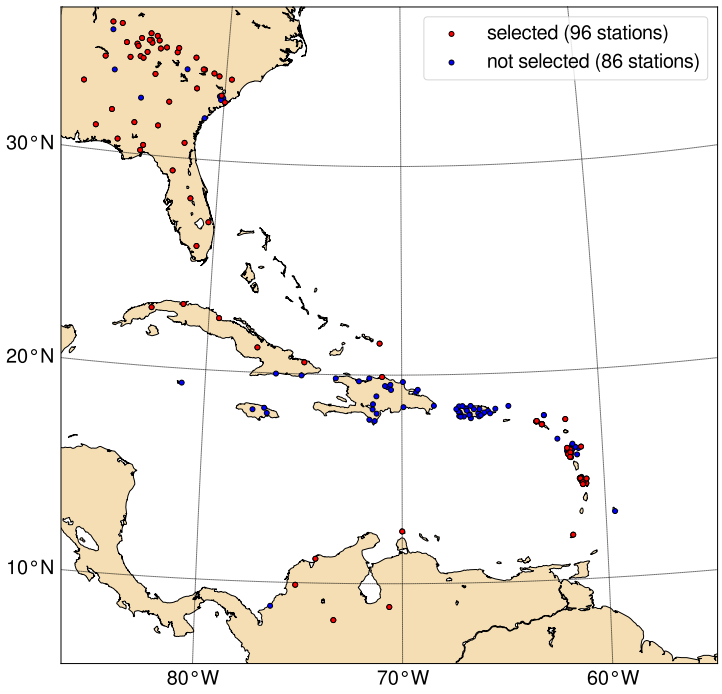

Figure S22: Seismic stations considered and selected (after quality control) for imaging the 2024 Mendocino $M_{\mathrm{w}}7$ earthquake with back-projection. Stations are selected based on the waveform similarity of their direct P-wave arrivals, with a network-average cross-correlation coefficient greater than 0.7 required for inclusion.

References

15. Goldberg, D. E., Koch, P., Melgar, D., Riquelme, S. & Yeck, W. L. Beyond the Teleseism: Introducing Regional Seismic and Geodetic Data into Routine USGS Finite-Fault Modeling. *Seismological Research Letters* **93,** 3308–3323. doi:10.1785/0220220047 (2022).

26. Stephenson, W. J., Reitman, N. G. & Angster, S. J. *P-and S-wave velocity models incorporating the Cascadia subduction zone for 3D earthquake ground motion simulations, Version 1.6—Update for Open-File Report 2007–1348* tech. rep. (US Geological Survey, 2017). doi:10.3133/ofr20171152.

50. Jennings, C. W. & Bryant, W. A. *Fault Activity Map of California* Geologic Data Map No. 6, scale 1:750,000. Version 2.0. California Geological Survey 150th Anniversary Edition. Sacramento, CA, 2010. https://maps.conservation.ca.gov/cgs/metadata/GDM_006_FAM_750k_v2_metadata.html.

55. Blewitt, G., Hammond, W. & Kreemer, C. Harnessing the GPS data explosion for interdisciplinary science. *Eos* **99,** e2020943118 (2018).